

# CEBAF Program Advisory Committee Nine Proposal Cover Sheet

This proposal must be received by close of business on Thursday, December 1, 1994 at:

CEBAF

User Liaison Office, Mail Stop 12 B

12000 Jefferson Avenue

Newport News, VA 23606

## Proposal Title

Photoproduction of the Rho Meson from the Proton with Linearly Polarized Photons

## Contact Person

Name:

J. P. Connelly

Institution:

The George Washington University  
Physics Department, Corcoran Hall

Address:

Address:

City, State ZIP/Country:

Washington, D.C. 20052 USA

Phone:

703-729-8345

FAX:

202-994-3001

E-Mail → Internet:

connelly@gwuvvm.gwu.edu

Experimental Hall: B

Days Requested for Approval: 20

Hall B proposals only, list any experiments and days for concurrent running:

## CEBAF Use Only

Receipt Date: 12/15/94

PR 94 - 109

By: JP

# Photoproduction of the $\rho$ Meson from the Proton with Linearly Polarized Photons

P.L. Cole,<sup>\*†</sup> J.P. Connelly,<sup>\*†</sup> B.L. Berman,

W.J. Briscoe, K.S. Dhuga, S.L. Rugari

*Center for Nuclear Studies, The George Washington University*

R.R. Whitney<sup>\*</sup>

*CEBAF*

S. Capstick

*Florida State University*

H. Crannell, S.K. Matthews, J. O'Brien, D.I. Sober

*The Catholic University of America*

J. Comfort, R. Alarcon

*Arizona State University*

J. Napolitano

*Rensselaer Polytechnic Institute*

J. Ficenec, D. Jenkins

*Virginia Polytechnic Institute*

G. Audit, M. Guidal, F. Kunne, J-M. Laget,

C. Marchand, L. Murphy, B. Saghai

*Service de Physique Nucléaire, Centre d'Etudes de Saclay*

C. Hyde-Wright, W. Roberts<sup>°</sup>

*Old Dominion University, °CEBAF*

D.M. Manley

*Kent State University*

\* Co-Spokesperson

† Contact person

‡ Will present proposal

## Abstract

The photoproduction of  $\rho^0$  and  $\rho^+$  mesons from the proton will be used to study the baryon resonance region between 1.66 and 2.22 GeV center-of-mass energy. The  $\rho N$  channel is known to be a significant branch for the decay of baryon resonances in this energy region. The measurement will employ a linearly polarized photon beam produced by coherent bremsstrahlung from a diamond crystal to measure the beam asymmetry and the spin density matrix elements of the two-pion decay of the  $\rho$  mesons. The spin density matrix elements and polarization asymmetry of the  $\rho$  decay will be extracted as functions of the squared four-momentum transfer  $t$  and the center-of-mass energy  $\sqrt{s}$ . This will facilitate the search for baryon resonance contributions and provide new physics information on diffractive,  $t$  and  $u$ -channel processes. The proposed experiment will probe the lower energy region ( $1.0 < E_\gamma < 1.5$  GeV) with an average photon polarization of 60% by using a 4 GeV electron beam. A second run with a 6 GeV electron beam will permit measurements in the energy regime  $1.4 < E_\gamma < 2.15$  GeV with an average photon polarization of 70%. The 100 MeV overlap will allow for cross checking and comparing the results of the two runs.

# 1 Introduction

We will measure the photoproduction of  $\rho$  mesons by using linearly polarized photons, emphasizing the production via  $\rho N$  decay of baryon resonances. The measurement of the complete angular distribution of the  $\rho$  meson and its decay products when photoproduced by linearly polarized photons will result in a set of rigid constraints necessary for the ultimate extraction of the masses, partial widths, and helicity amplitudes of those resonances decaying via the  $\rho N$  channel.

The quantities to be measured in this experiment are the spin density matrix elements of the  $\rho$  meson. These observables, three from unpolarized photoproduction experiments and six additional ones with a linearly polarized photon beam, are extracted *in the rest frame of the  $\rho$*  by measuring the polar and azimuthal angular distributions of the decay  $\pi^+$  referenced with respect to the orientation of the photon spin. Data to be obtained over the full  $\theta_{\text{lab}}$  range and over a large incident photon energy range will allow us to extract the spin density matrix elements as functions both of the square of the four-momentum transfer  $t$  and of the c.m. energy  $\sqrt{s}$ . By using CLAS, the photon tagger and a continuous electron beam, we will be in the exciting position to perform these measurements with full angular coverage, low systematic uncertainties and high statistics.

Linearly polarized photons at high energies have been used to determine the natural parity character of the pomeron exchange in the Vector Dominance Model. At resonance energies ( $< 2.4$  GeV), the high energy approximation used to separate natural and unnatural parity exchange no longer holds. Instead, the coupling of the excited baryon is now sensitive to the spin of the incident photon. Unlike diffractive  $\rho$  photoproduction, the spin of the photon is not directly transmitted to the  $\rho$  meson. We expect to see a much different behavior of the spin density matrix elements at energies where resonance contributions are important compared with higher energies.

Processes other than resonance formation will also contribute to the  $\rho$  photoproduction cross section. The diffractive and  $t$ -channel exchange contributions, for example, will dominate the cross section at low  $t$ , while  $u$ -channel exchange will be large at high  $t$ . These processes are of interest in their own right and interference effects with resonant  $\rho$  photoproduction may well be a significant effect. We will be measuring over the full kinematical range in  $t$  and thus will be sensitive to all of these processes.

## 2 Motivation

The spectrum of excited states of a system of bound particles provides a window to the underlying interaction. Just as in nuclear spectroscopy, where the excited-state spectrum reflects the quantum many-body configurations of nucleons and mesons interacting via the strong nuclear force, so does baryon spectroscopy afford us the opportunity to study the interaction of quarks and gluons in excited states.

An important motivation for studying the spectrum of baryon resonances with photons is to obtain information on the photoproduction amplitudes of the individual resonances. Most of our knowledge of the baryon resonance spectrum has come from the reactions  $\pi N \rightarrow \pi N$ ,  $\gamma N \rightarrow \pi N$ , and  $\pi N \rightarrow \pi\pi N$ . At center-of-mass energies below 1.7 GeV, the single pion production channel dominates both the pion and photoabsorption cross sections. As the c.m. energy increases towards 2.0 GeV the two-pion decay channel becomes more dominant, and it is in this important energy region that the masses and partial widths of the resonances are poorly determined.

An outstanding problem in our current day understanding of baryon spectroscopy is that of the missing resonances. For example, the SU(6) symmetric quark model predicts many more resonances than have been thus far observed. One solution is to restrict the number of internal degrees of freedom by assuming that two quarks are bound in a diquark pair [1], thus lowering the level density of baryon resonances. An alternate solution has been put forward by Koniuk and Isgur [2] and others [3],[4]. In these calculations it has been found that the missing resonances tend to couple weakly to the  $\pi N$  channel and strongly to the  $\pi\pi N$  channel. Since most of our information on the baryon resonance spectrum comes from partial-wave analyses of  $\pi N \rightarrow \pi N$  measurements, the reason for these ‘missing states’ may be purely an experimental problem. The models predict that these resonances will have a reasonable coupling to the photon. For this reason, several approved CEBAF photoproduction [5] and electroproduction [6] experiments using unpolarized probes will search for resonances decaying via  $\rho N$  and other two-pion decay channels. We expect the identification of many of these resonances, with their broad widths and narrow spacing, to be difficult. The sensitivity afforded by linearly polarized photons will provide additional constraints in identifying these resonances.

Experimentally, several difficulties are immediately apparent. The number of resonances

extracted either from the analyses of pion production data or from the theoretical predictions is large. In addition, the resonance widths are broad (typically  $\sim 150$  MeV), and one is faced with the problem of disentangling many overlapping resonances. In general, a complete phase-shift analysis is required to extract the helicity amplitudes for the various resonances. An analysis of this sort demands both unpolarized photoproduction data, and a complete set of polarization experiments in order to extract fundamental information from the set of bilinear combinations of helicity amplitudes obtained from any one of these experimental conditions.

There have been several independent partial-wave analyses of the reactions  $\pi N \rightarrow \pi N$  and  $\gamma N \rightarrow \pi N$  [7], [8]. There have also been isobar-model partial-wave analyses for the reaction  $\pi N \rightarrow \pi\pi N$ . The Kent State multichannel resonance analysis has been published [9], and an extensive review of the  $\pi N \rightarrow \pi\pi N$  analyses can be found in Ref. [10]. To our knowledge, no such analysis has been performed for  $\gamma N \rightarrow \pi\pi N$ .

The analysis of the  $\gamma N \rightarrow \pi\pi N$  reaction involves *six* isospin amplitudes. If the analysis is restricted to the  $\rho N$  decay channel only, the number of isospin amplitudes contributing in the partial-wave analysis reduces to three; however, the analysis of this reaction is further complicated by the nonzero spin of the  $\rho$  meson. Since there are more ways that a spin-1 particle can couple to the nucleon than can a spin-0 particle, there will be a greater number of partial waves for a given I, J, and parity. It is clear from the large number of amplitudes that would be required for such an analysis that complete sets of data are necessary, including cross sections, angular distributions from both unpolarized and polarized photoproduction experiments, and polarized target data.

### 3 Physics

#### 3.1 The Decay Angular Distribution

The goal of the proposed experiment is to measure the reactions  $\gamma p \rightarrow \rho^0 p$  and  $\gamma p \rightarrow \rho^+ n$  by using linearly polarized photons in the energy range of  $1.0 \leq E_\gamma \leq 2.15$  GeV. In a practical sense, we will be measuring the spin density matrix elements  $\rho_{\alpha\beta}^n$  which determine the angular distribution of the two-pion decay of the  $\rho$  meson. The upper index is related to photon spin by the Pauli spin matrices,

$$(\rho^0, \rho^n) = H(\frac{1}{2}\mathbf{I}, \frac{1}{2}\sigma^n)H^\dagger \quad n = 1, 2, 3$$

where  $H$  is the helicity amplitude matrix. The lower indices of  $\rho_{\alpha\beta}^n$ ,  $\alpha, \beta = -1, 0, 1$ , correspond to the possible helicity states of the vector meson. The complete angular distribution  $W(\cos\theta, \phi, \Phi)$  is given by [11],

$$\begin{aligned} W(\cos\theta, \phi, \Phi) = & W^0(\cos\theta, \phi, \rho_{\alpha\beta}^0) - P_\gamma \cos 2\Phi W^1(\cos\theta, \phi, \rho_{\alpha\beta}^1) \\ & - P_\gamma \sin 2\Phi W^2(\cos\theta, \phi, \rho_{\alpha\beta}^2) \end{aligned} \quad (1)$$

where

$$\begin{aligned} W^0(\cos\theta, \phi, \rho_{\alpha\beta}^0) &= \frac{3}{4\pi} \left[ \frac{1}{2} \sin^2 \theta + \frac{1}{2} (3 \cos^2 \theta - 1) \rho_{00}^0 \right. \\ &\quad \left. - \sqrt{2} \operatorname{Re} \rho_{10}^0 \sin 2\theta \cos \phi - \rho_{1-1}^0 \sin^2 \theta \cos 2\phi \right] \\ W^1(\cos\theta, \phi, \rho_{\alpha\beta}^1) &= \frac{3}{4\pi} \left[ \rho_{11}^1 \sin^2 \theta + \rho_{00}^1 \cos^2 \theta \right. \\ &\quad \left. - \sqrt{2} \operatorname{Re} \rho_{10}^1 \sin 2\theta \cos \phi - \rho_{1-1}^1 \sin^2 \theta \cos 2\phi \right] \\ W^2(\cos\theta, \phi, \rho_{\alpha\beta}^2) &= \frac{3}{4\pi} \left[ \sqrt{2} \operatorname{Im} \rho_{10}^2 \sin 2\theta \sin \phi + \operatorname{Im} \rho_{1-1}^2 \sin^2 \theta \sin 2\phi \right] \end{aligned}$$

$\theta$  and  $\phi$  are the polar and azimuthal angles of the  $\pi^+$  decay product in the helicity reference frame<sup>1</sup> and  $P_\gamma$  is the degree of linear polarization of the photon beam. Shown in Fig. 1 is the graphical depiction of these angles. Thus, with linearly polarized photons, one has access to six more independent spin density matrix elements than can be obtained in an unpolarized vector meson photoproduction experiment. By using CLAS, we will measure

---

<sup>1</sup>The  $z$ -axis is defined as the direction opposite the proton in the total c.m. system. The direction of the decay  $\pi^+$  in the  $\rho$  rest frame defines the polar angle  $\theta$  and the azimuthal angle  $\phi$  (with respect to the production plane);  $\Phi$  is the angle between the photon polarization vector and the production plane.

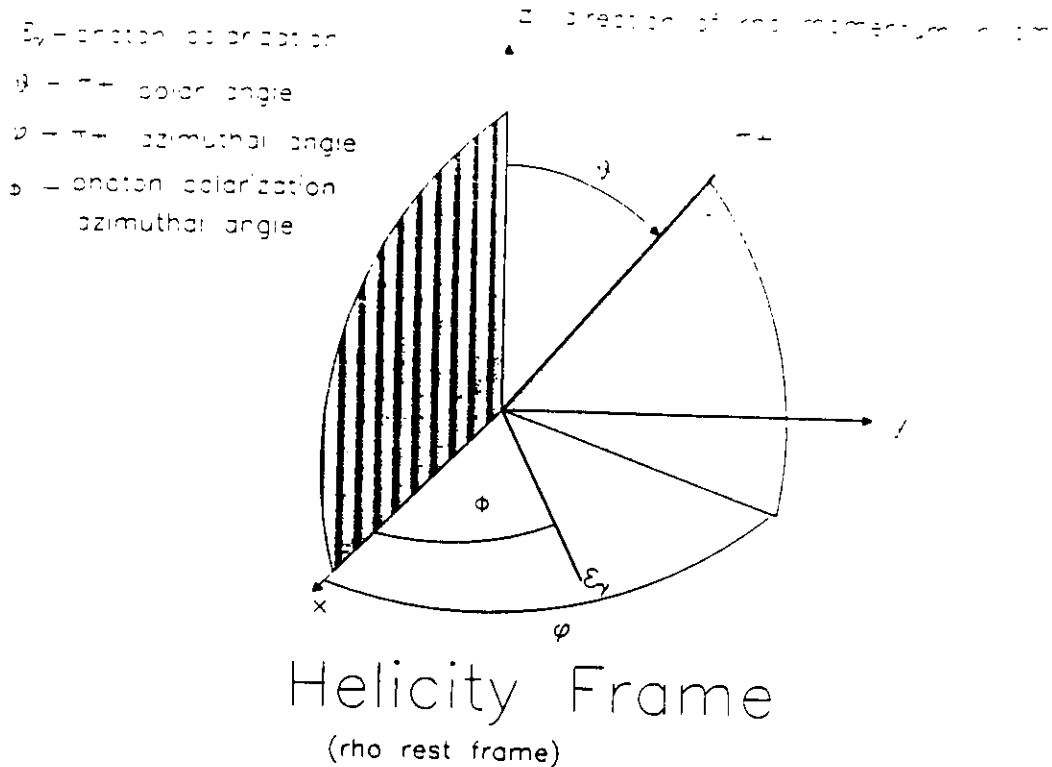


Figure 1: Helicity reference frame.  $\Phi$  is the azimuthal angle of the electric vector  $\vec{\epsilon}$  of the photon, and  $\theta$  and  $\phi$  are the polar and azimuthal angles of the decay  $\pi^+$ .

the angular distribution (and hence the spin density matrix elements) of the  $\rho$  production both as a function of  $t$  and of the incident photon energy.

The density matrix elements from diffractive photoproduction have been measured previously in bubble-chamber experiments, using a linearly polarized photon beam at SLAC [12] with photon energies of 2.8 and 4.7 GeV for  $|t| \leq 0.4 \text{ (GeV/c)}^2$ . The measured density matrix elements at these kinematics give rise to an angular dependence that is characteristic of natural-parity exchange (pomeron exchange) in the  $t$  channel and of  $s$ -channel helicity conservation, as one would expect if the helicity of the vector meson mimics that of a real photon. Shown in Fig. 2 are the SLAC data, displayed as a function of  $\cos\theta$  and as a function of  $\psi = \phi - \Phi$  (with  $\theta, \phi, \Phi$  as defined in the footnote on page 5). For a polarization of  $P_\gamma = 1$ ,  $s$ -channel helicity conservation demands that the two-pion products of the  $\rho^0$  have a decay angular distribution given by  $\sin^2\theta \cos 2\psi$ , and this is reflected in the data. The decay products from the  $\rho$  decay lie preferentially in the plane where  $\Phi$ , the angle made by the photon electric polarization vector and the production plane, is equal to the azimuthal decay angle of the  $\pi^+$ .



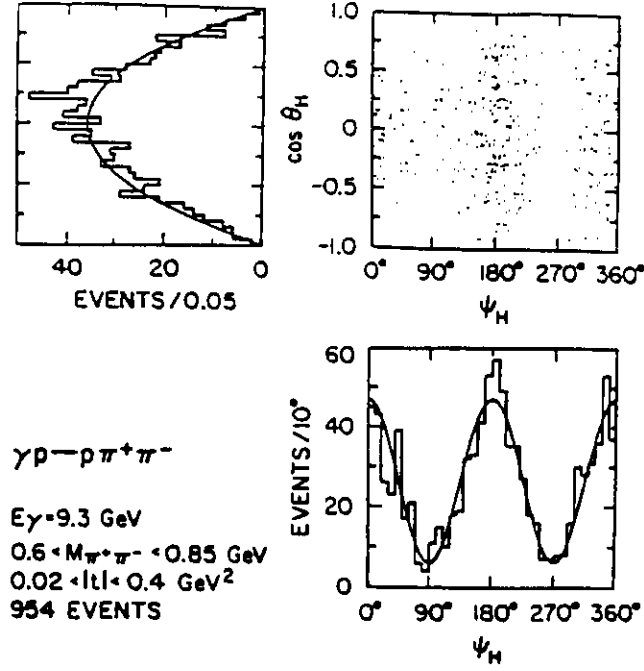


Figure 2: Angular distributions of decay pions for low- $|t|$  data from SLAC [9] in  $\bar{\gamma}p \rightarrow \rho^0 p$ .

Another way to determine this feature is to measure the photon asymmetry parameter

$$\Sigma \equiv \frac{\sigma_{\parallel} - \sigma_{\perp}}{\sigma_{\parallel} + \sigma_{\perp}}.$$

Here  $\sigma_{\parallel}$  ( $\sigma_{\perp}$ ) is the cross section for the pions from  $\rho^0$  decay ( $\theta = \pi/2, \phi = \pi/2$ ), to emerge in the plane of the photon polarization (or perpendicular to it). In terms of the differential cross section,  $W(\cos \theta, \phi, \Phi)$ ,  $\Sigma$  can be recast as

$$\Sigma = \frac{W(\cos \frac{\pi}{2}, \frac{\pi}{2}, \frac{\pi}{2}) - W(\cos \frac{\pi}{2}, \frac{\pi}{2}, 0)}{W(\cos \frac{\pi}{2}, \frac{\pi}{2}, \frac{\pi}{2}) + W(\cos \frac{\pi}{2}, \frac{\pi}{2}, 0)}.$$

This asymmetry can be rewritten in terms of the measurable density matrix elements as

$$\Sigma = P_{\gamma} \frac{2(\rho_{11}^1 + \rho_{1-1}^1)}{1 - \rho_{00}^0 + 2\rho_{1-1}^0}. \quad (2)$$

For purely diffractive  $\rho^0$  photoproduction,  $\Sigma = 1$ . Any deviation from this value is an indication that nondiffractive processes are present.

### 3.2 Density Matrix Elements and Helicity Amplitudes

The meeting ground between experiment and theories predicting the baryon excitation spectrum is the helicity amplitudes. Following the formalism of Ref. [13], we note there are six

independent helicity amplitudes of  $\gamma p \rightarrow \rho N$ ,  $H_{\lambda_\rho \lambda_p, \lambda_\gamma \lambda_N}(\sqrt{s}, \theta, \phi)$ . These helicity amplitudes can be expanded in terms of the parity-conserving partial-wave helicity conserving amplitudes,  $H_{\lambda_\rho \lambda_p, \lambda_\gamma \lambda_N}^{J\pm}(\sqrt{s})$ , where the  $\pm$  has to be chosen to be equal to  $+$  or  $-$ , depending upon whether the parity is equal to  $+(-1)^{J-\frac{1}{2}}$  or to  $-(-1)^{J-\frac{1}{2}}$ . For the sake of brevity, we write

$$\begin{aligned} H_1^{J\pm} &= H_{\frac{1}{2}, \frac{1}{2}}^{J\pm} & H_2^{J\pm} &= H_{\frac{1}{2}, 1-\frac{1}{2}}^{J\pm} \\ H_3^{J\pm} &= H_{-\frac{1}{2}, \frac{1}{2}}^{J\pm} & H_4^{J\pm} &= H_{-\frac{1}{2}, 1-\frac{1}{2}}^{J\pm} \\ H_5^{J\pm} &= H_{\frac{0}{2}, \frac{1}{2}}^{J\pm} & H_6^{J\pm} &= H_{\frac{0}{2}, 1-\frac{1}{2}}^{J\pm} \end{aligned}$$

The relationship between the spin density matrix elements and the helicity amplitudes can be determined explicitly. Table 1 lists the helicity amplitude dependence of the spin density matrix elements. As an example, we explicitly write out two of the six linearly polarized density matrix elements,<sup>2</sup>  $\rho_{11}^1$  and  $\rho_{1-1}^1$ , which appear in the numerator of the asymmetry parameter  $\Sigma$  (see eq. 2). Clearly, high quality measurements of these matrix elements, accessible in a linearly polarized photon experiment, will severely constrain any analysis seeking to extract the helicity amplitudes for this reaction.

In a simple model calculation, Roberts [14] treats the process  $\gamma N \rightarrow \rho N$ . The four processes that are involved in  $\rho$ -meson photoproduction are depicted in Fig. 3: diffractive scattering,  $t$ -channel exchange,  $u$ -channel exchange and production of  $\rho$ -mesons via the decay of an  $s$ -channel resonance. Of these, only  $s$ -channel exchange of baryon resonances is assumed; the model is intended simply to illustrate what might be observed due to  $s$ -channel resonances. For this calculation, the predicted resonances with  $J^P = 1/2^\pm$ ,  $3/2^\pm$ , and  $5/2^\pm$  [3] are used. This means that there are 26 states, listed in Table 2, that contribute to the amplitudes. Note that of these 26 predicted states, only 11 are well established (as indicated by the \*\*\*\* rating) and several have not yet been observed. More details of the

---

<sup>2</sup>The density matrix elements can be written in terms of the incident photon energy  $E_\gamma$ , the total angular momentum  $J$ , and the partial-wave helicity amplitudes,  $H_i$ . For example

$$\begin{aligned} \rho_{11}^1 &= \sum_J \frac{(2J+1)^2}{32E_\gamma^2} \text{Re}(H_1 H_2^*) \{d_{\frac{1}{2}\frac{1}{2}}^J d_{-\frac{1}{2}\frac{1}{2}}^J e^{2i\phi} - d_{-\frac{1}{2}\frac{1}{2}}^J d_{\frac{1}{2}\frac{1}{2}}^J e^{-2i\phi}\} + \text{Re}(H_3 H_4^*) \{d_{\frac{1}{2}\frac{3}{2}}^J d_{-\frac{3}{2}\frac{3}{2}}^J e^{2i\phi} - d_{-\frac{1}{2}\frac{3}{2}}^J d_{\frac{3}{2}\frac{3}{2}}^J e^{-2i\phi}\} \\ \text{and} \\ \rho_{1-1}^1 &= \sum_J \frac{(2J+1)^2}{32E_\gamma^2} \text{Re}(H_1 H_4^*) \{d_{\frac{1}{2}\frac{1}{2}}^J d_{\frac{3}{2}\frac{3}{2}}^J - d_{-\frac{1}{2}\frac{1}{2}}^J d_{-\frac{3}{2}\frac{3}{2}}^J e^{-4i\phi}\} + \text{Re}(H_2 H_3^*) \{(d_{\frac{1}{2}\frac{3}{2}}^J)^2 + (d_{-\frac{1}{2}\frac{3}{2}}^J)^2 e^{-4i\phi}\}. \end{aligned}$$

Here, the  $d_{\lambda_\gamma - \lambda_N, \lambda_\rho - \lambda_{N'}}^J$  are the Wigner rotation functions.

Table 1: Partial-wave helicity amplitudes that go into a given density matrix element.  $H_i$  stands for  $H_i^{J\pm}$  ( $i = 1, \dots, 6$ ).

$\rho_{\alpha\beta}^n$	Partial-Wave Helicity Amplitudes
$\rho_{00}^0$	$ H_5 ^2,  H_6 ^2$
$\rho_{10}^0$	$\text{Re}(H_1 H_5^*), \text{Re}(H_2 H_6^*), \text{Re}(H_3 H_5^*), \text{Re}(H_4 H_6^*)$
$\rho_{1-1}^0$	$H_1 H_3^*, H_2 H_4^*$
$\rho_{00}^1$	$\text{Re}(H_5 H_6^*)$
$\rho_{11}^1$	$\text{Re}(H_1 H_2^*), \text{Re}(H_3 H_4^*)$
$\rho_{1-1}^1$	$\text{Re}(H_1 H_4^*), \text{Re}(H_2 H_3^*)$
$\rho_{10}^1$	$H_1 H_6^*, H_2 H_5^*, H_3 H_6^*, H_4 H_5^*$
$\rho_{1-1}^2$	$i\text{Re}(H_1 H_4^*), i\text{Re}(H_2 H_3^*)$
$\rho_{10}^2$	$iH_1 H_6^*, iH_2 H_5^*, iH_3 H_6^*, iH_4 H_5^*$

models used to calculate these couplings and masses can be found in Refs. [3],[4],[15], and [16]. Further details of the photoproduction model calculation can be found in Ref. [14].

As an example, the calculated asymmetry  $\Sigma$  from this model for the process  $\gamma N \rightarrow N_{\frac{3}{2}}^{3+}(1910) \rightarrow \rho N$ , where  $N_{\frac{3}{2}}^{3+}(1910)$  is the single  $\frac{3}{2}^+$  state at 1910 MeV, is shown in Fig. 4. Two cases are displayed. The  $\rho N$  decay of the  $N_{\frac{3}{2}}^{3+}(1910)$  resonance can be expanded into three partial waves, one of which has an amplitude nine times greater than the other two. The differences between the two curves arise only from the changing of the sign of this largest amplitude. Clearly, in this model, the polarization asymmetry is sensitive to the underlying physics.

Using the model by Roberts, we have calculated three cases: 1) all twenty-six resonances included; 2) none of the missing resonances included except for the  $N_{\frac{3}{2}}^{3+}(1910)$ ; and 3) all of the missing resonances included except for the  $N_{\frac{3}{2}}^{3+}(1910)$ . Figure 5 shows two of the six  $\rho$  decay density matrix elements ( $\rho_{11}^1$  and  $\rho_{1-1}^1$ ) that one obtains by using linearly polarized photons at three different c.m. energies. We observe in eq. 2 that the numerator of  $\Sigma$  is formed of the sum of these two density matrix elements. The effect of the  $N_{\frac{3}{2}}^{3+}(1910)$  is most dramatic at the resonance centroid energy and at  $\theta_{\text{cm}} = 90^\circ$ . This is precisely the kinematical

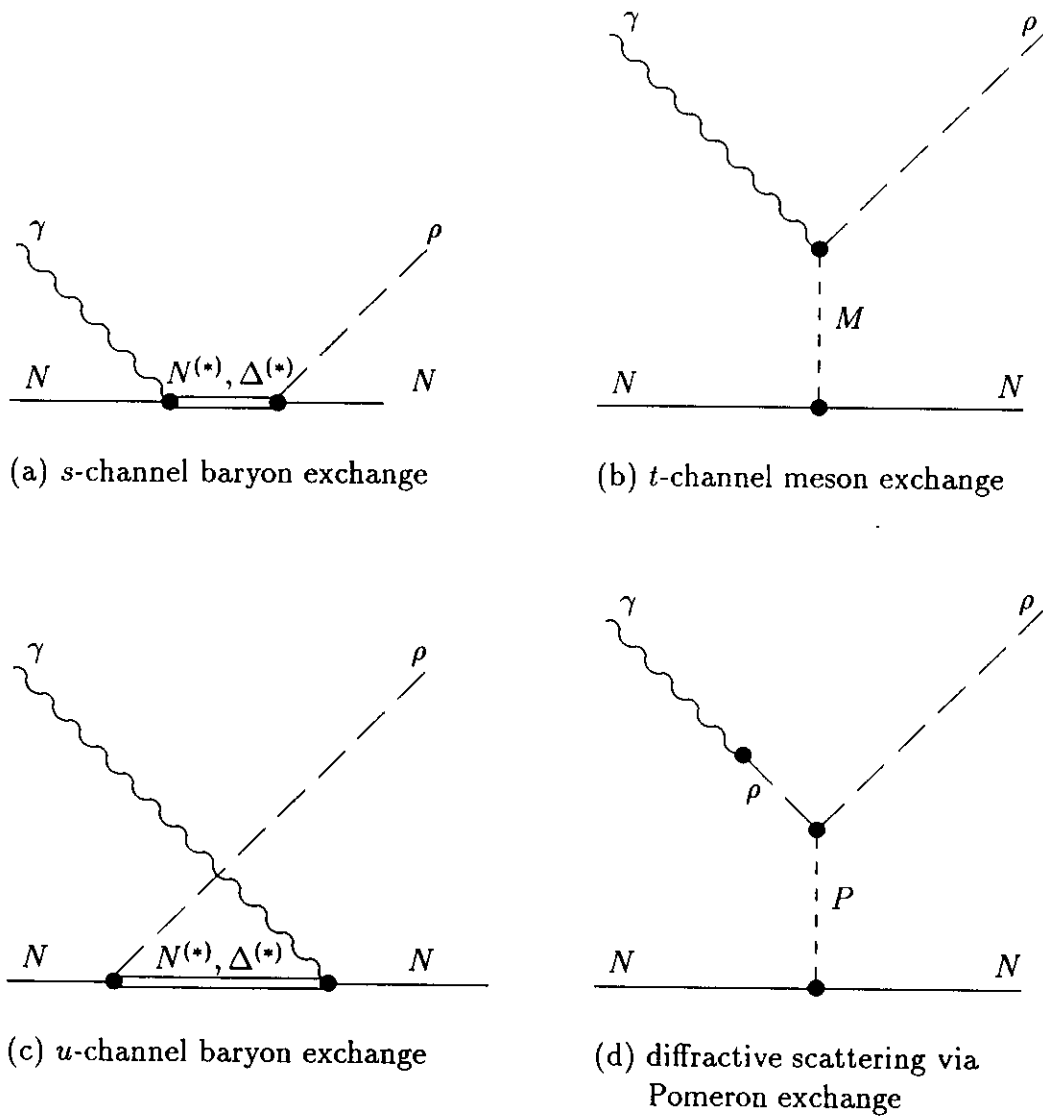


Figure 3: Processes involved in  $\rho$ -meson photoproduction.

Table 2: States that are used in the model calculation. States from the partial-wave analyses are listed (along with their overall rating) in the same row as our model state assignment. ‘Missing’ states are those with no experimentally observed analogs.

model state	$N\pi$ state assignment	rating
$[N_{\frac{1}{2}}^{-}]_1(1460)$	$N_{\frac{1}{2}}^{-}(1535)$	****
$[N_{\frac{1}{2}}^{-}]_2(1535)$	$N_{\frac{1}{2}}^{-}(1650)$	****
$[N_{\frac{3}{2}}^{-}]_1(1495)$	$N_{\frac{3}{2}}^{-}(1520)$	****
$[N_{\frac{3}{2}}^{-}]_2(1625)$	$N_{\frac{3}{2}}^{-}(1700)$	***
$[N_{\frac{5}{2}}^{-}]_1(1630)$	$N_{\frac{5}{2}}^{-}(1675)$	****
$[N_{\frac{1}{2}}^{+}]_2(1540)$	$N_{\frac{1}{2}}^{+}(1440)$	****
$[N_{\frac{1}{2}}^{+}]_3(1770)$	$N_{\frac{1}{2}}^{+}(1710)$	***
$[N_{\frac{1}{2}}^{+}]_4(1880)$		
$[N_{\frac{1}{2}}^{+}]_5(1975)$		
$[N_{\frac{3}{2}}^{+}]_1(1795)$	$N_{\frac{3}{2}}^{+}(1720)$	****
$[N_{\frac{3}{2}}^{+}]_2(1870)$		
$[N_{\frac{3}{2}}^{+}]_3(1910)$		
$[N_{\frac{3}{2}}^{+}]_4(1950)$		
$[N_{\frac{3}{2}}^{+}]_5(2030)$		
$[N_{\frac{5}{2}}^{+}]_1(1770)$	$N_{\frac{5}{2}}^{+}(1680)$	****
$[N_{\frac{5}{2}}^{+}]_2(1980)$	$N_{\frac{5}{2}}^{+}(2000)$	**
$[N_{\frac{5}{2}}^{+}]_3(1995)$		
$[\Delta_{\frac{1}{2}}^{-}]_1(1555)$	$\Delta_{\frac{1}{2}}^{-}(1620)$	****
$[\Delta_{\frac{3}{2}}^{-}]_1(1620)$	$\Delta_{\frac{3}{2}}^{-}(1700)$	****
$[\Delta_{\frac{1}{2}}^{+}]_1(1835)$		
$[\Delta_{\frac{1}{2}}^{+}]_2(1875)$	$\Delta_{\frac{1}{2}}^{+}(1910)$	****
$[\Delta_{\frac{3}{2}}^{+}]_2(1795)$	$\Delta_{\frac{3}{2}}^{+}(1600)$	**
$[\Delta_{\frac{3}{2}}^{+}]_3(1915)$	$\Delta_{\frac{3}{2}}^{+}(1920)$	***
$[\Delta_{\frac{3}{2}}^{+}]_4(1985)$		
$[\Delta_{\frac{5}{2}}^{+}]_1(1910)$	$\Delta_{\frac{5}{2}}^{+}(1905)$	****
$[\Delta_{\frac{5}{2}}^{+}]_2(1990)$	$\Delta_{\frac{5}{2}}^{+}(2000)$	**

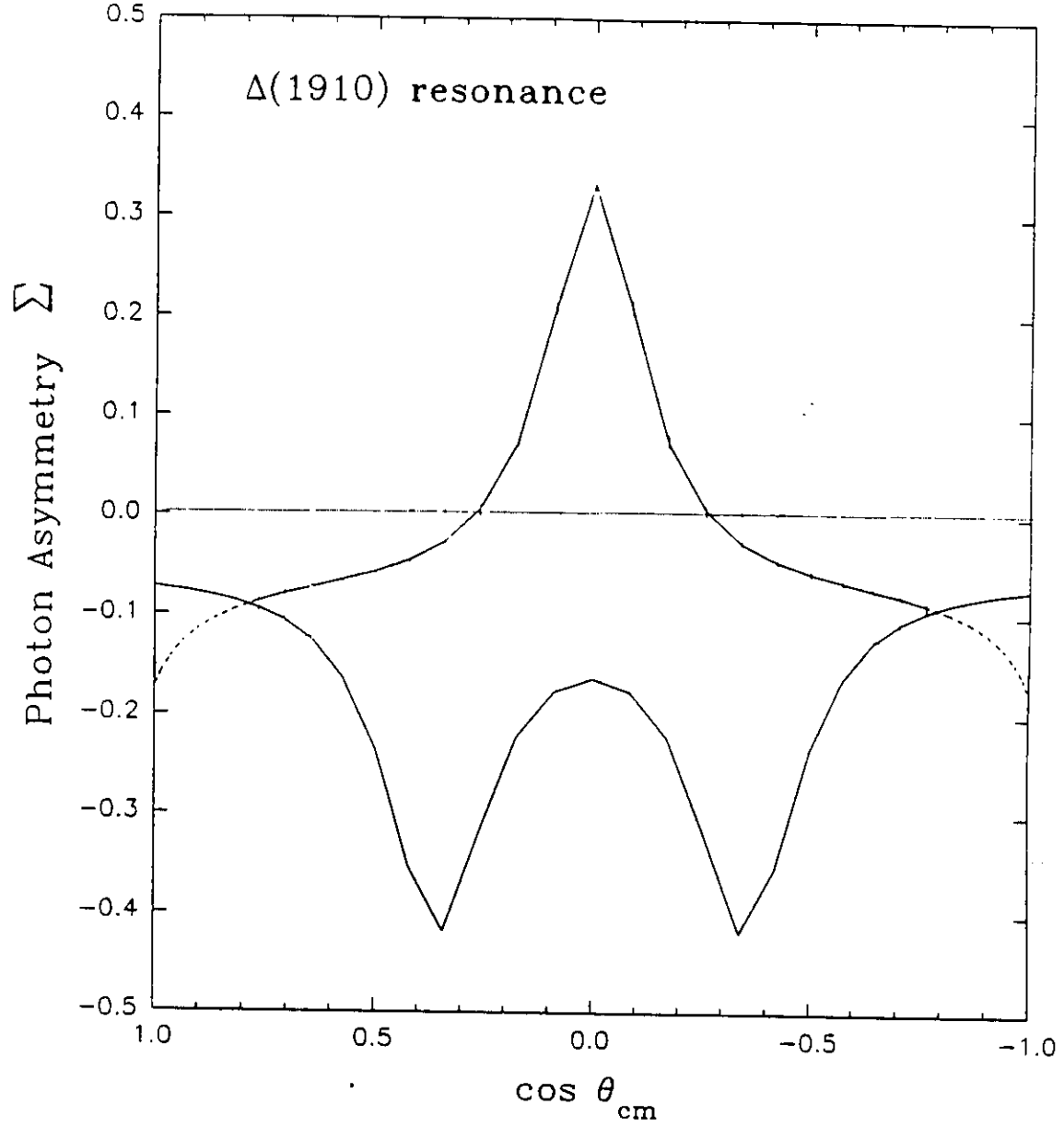


Figure 4: The photon asymmetry  $\Sigma$  for the  $N_{\frac{3}{2}}^{+}(1910)$  calculated by Roberts [14]. The two curves are for the same asymmetry but with a sign change in the dominant partial wave amplitude.

region where the nonresonant backgrounds, which arise from diffractive scattering and  $t$  and  $u$ -channel processes, have been reduced the most.

### 3.3 $u$ -channel processes

From the duality principle, the cross section for  $\rho$  photoproduction can be calculated, in principle, by summing over all possible  $t$ -channel meson-exchange processes [Fig. 3(b)], or over all possible  $s$ -channel *plus* all possible  $u$ -channel baryon-exchange processes. The pomeron exchange contribution to diffractive scattering of Fig. 3(d) needs to be added as a special case, as the effects of pomeron exchange in the  $t$ -channel are understood to be in addition to those of meson exchange. It is obviously more efficient to sum over  $t$ -channel exchange processes when in the diffractive (low- $t$ ) region, as a sum over  $s$  plus  $u$ -channel processes will require a large number of intermediate baryon states for convergence. Similarly, in the resonance region a  $t$ -channel sum will yield only the average cross section and will not show the characteristic energy dependence attributed to baryon resonances.

Constructing the cross section from a model, and likewise extracting resonance parameters from an analysis of the cross section, will therefore require different approaches in different kinematical regions. The  $s$ -channel sum used here by Roberts for an estimate of the resonance region cross section needs to be supplemented by the terms representing the  $u$ -channel diagrams of Fig. 3(c). If we work within time-ordered perturbation theory, in lowest order these diagrams will be suppressed relative to the  $s$ -channel diagrams because of energy denominators which are increased by the presence of the initial photon and the final  $\rho$  in the intermediate state. For a given intermediate baryon resonance, the  $\sqrt{s}$  for which the denominator is minimized, is pushed up to a higher value, and the minimum attained is significantly larger, relative to the  $s$ -channel diagram.

A coherent sum of such  $u$ -channel diagrams has been shown to possess a peak in backward directions for the similar process of Compton scattering from the nucleon [17], as seen in the  $\rho$  photoproduction data at high  $t$  values. This demonstrates the need for such diagrams if we are to model the cross section at all values of  $s$  and  $t$  of interest in this experiment. It is our intention [18] to build a more sophisticated model of resonance-region  $\rho$  photoproduction which builds on that of Roberts reported on here by the addition of these diagrams.

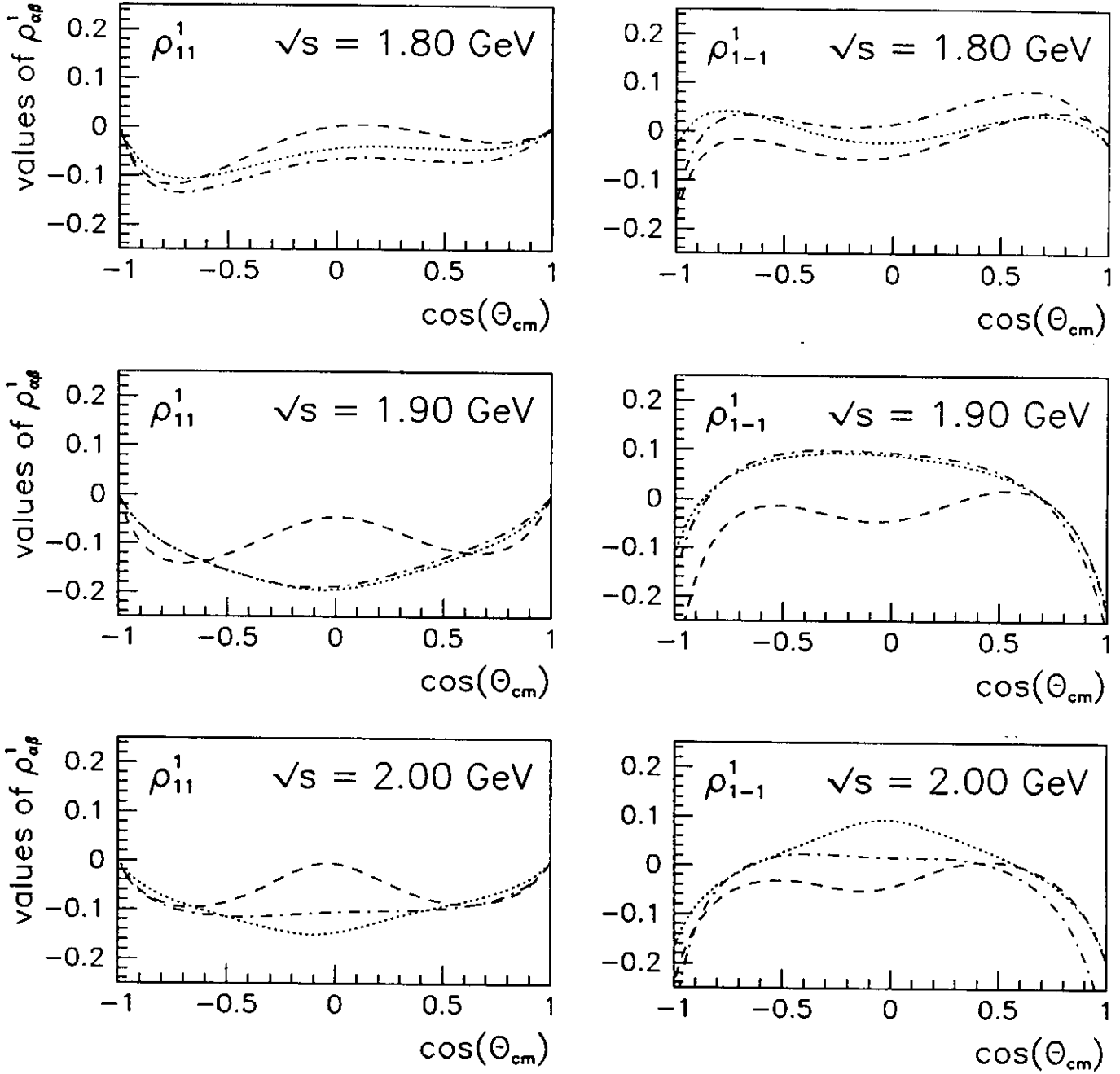


Figure 5: Predictions of the theory by Roberts [14]: (dashed line) only one missing resonance included; (dashed-dotted line) all but one of the missing resonances included; and (dotted line) all missing resonances included.



### 3.4 Previous Measurements

The combined cross section for diffractive and  $t$ -channel exchange  $\rho^0$  photoproduction peaks at forward angles with a  $t$  dependence given by  $d\sigma/dt = Ae^{-B|t|}$ . The contribution from the  $u$ -channel exchange term peaks at backward angles. Data obtained at 3.5, 4.0, and 6.0 GeV show that the backward angle cross section is described by  $d\sigma/du = Ce^{-D|u|}$  [19],[21].

Many experiments have been performed on the photoproduction of the  $\rho^0$ , including some polarization experiments. Most of these experiments were performed at a photon energy of 3 GeV or greater, but at very low  $t$ . The experiments performed with linearly polarized photon beams at SLAC [12] used a bubble chamber detector and hence suffered from low statistics. The results from this experiment can be explained purely in terms of the Vector Dominance Model as if the reaction proceeds almost entirely through natural-parity exchange in the  $t$  channel and is  $s$ -channel helicity conserving, as would be expected from diffractive photoproduction. Very few data exist in the energy regime near  $\sqrt{s} = 2.0$  GeV or lower or at a  $|t|$  much larger than  $0.4 \text{ (GeV/c)}^2$ . The data shown in Fig. 6 were obtained with a continuous bremsstrahlung beam. Shown in Fig. 7 are data [19] taken over the full  $t$ -range at  $E_\gamma = 4.0$  GeV, showing the exponential fall-off from the low- $t$  processes, a minimum (usually near  $\theta_{\text{cm}} = 90^\circ$ ), and the rise in the cross section at high  $t$  due to  $u$ -channel exchange. Figure 8 shows an extrapolation of the high-energy data to  $E_\gamma = 1.6$  GeV using the measured  $s$ -dependence from Ref. [19].

In the photon energy regime near 1.6 GeV ( $\sqrt{s} = 1.95$  GeV), one would expect to see some indication of resonance production. Data taken at DESY by two separate groups [22], [23] are plotted in Fig. 6 (averaging over the photon energy range of  $1.4 < E_\gamma < 1.8$  GeV) and compared with the high-energy extrapolation [19]. The agreement between the data and the curve is good for  $|t| < 0.5 \text{ (GeV/c)}^2$  and also for the high- $t$  data point. In the central region, near  $\theta_{\text{cm}} = 90^\circ$ , however, the data show an *enhancement by an order of magnitude* over the extrapolated curve. We therefore expect that our sensitivity to resonant photoproduction of the  $\rho$  meson will be enhanced in the region near  $\theta_{\text{cm}} = 90^\circ$ .

To study the  $\rho$  photoproduction in the absence of a diffractive background, one can turn to the charge exchange reaction  $\gamma p \rightarrow \rho^+ n$ . Although the data for this reaction are sparse, we expect an increase of the interval in  $t$  for which the resonant cross section is a large percentage of the total. This is due primarily to the lowering of the low- $t$  nonresonant

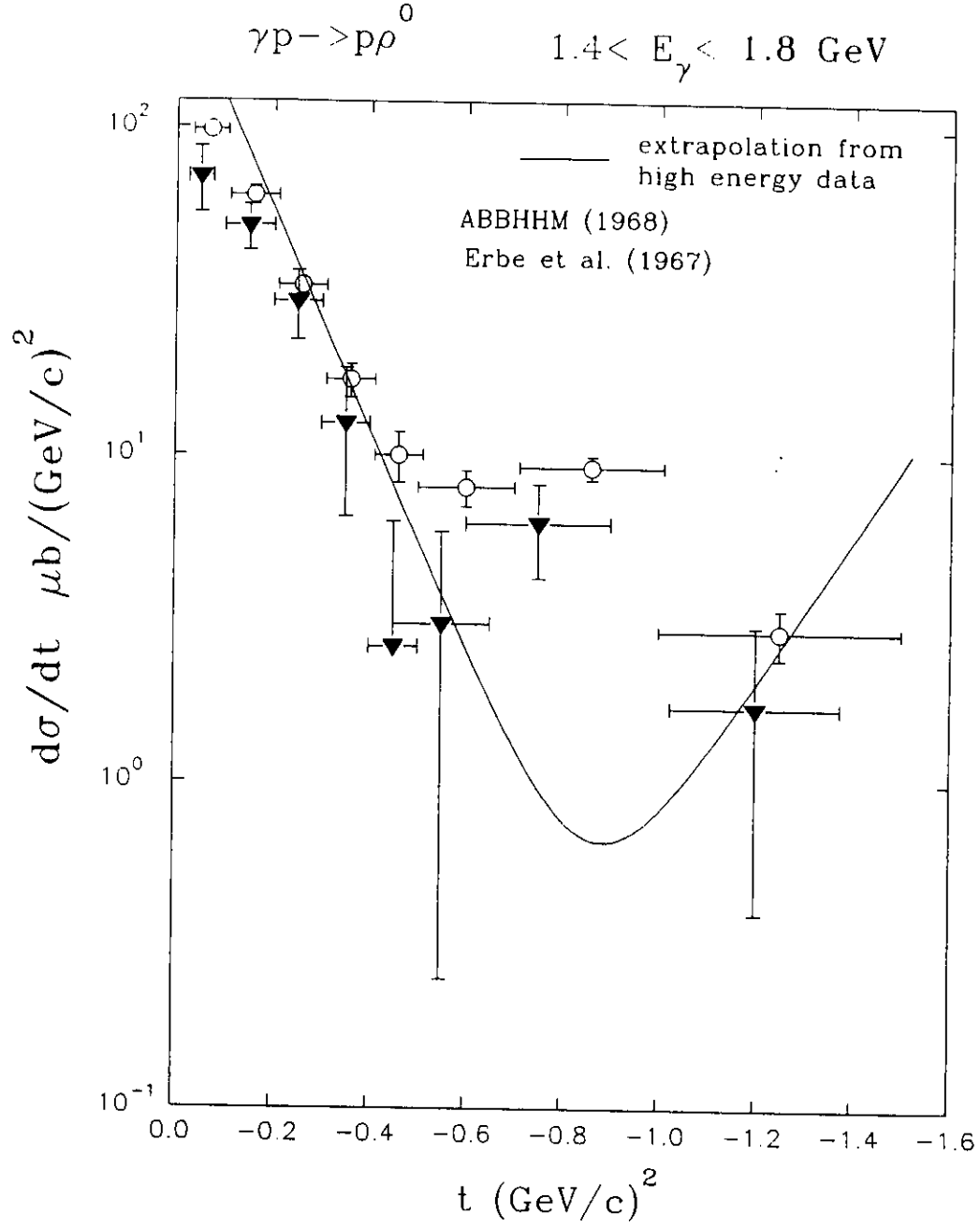


Figure 6: Comparison of a high-energy extrapolation to data [22], [23] in the regime of  $1.4 < E_\gamma < 1.8 \text{ GeV}$  for  $\gamma p \rightarrow \rho^0 p$ .

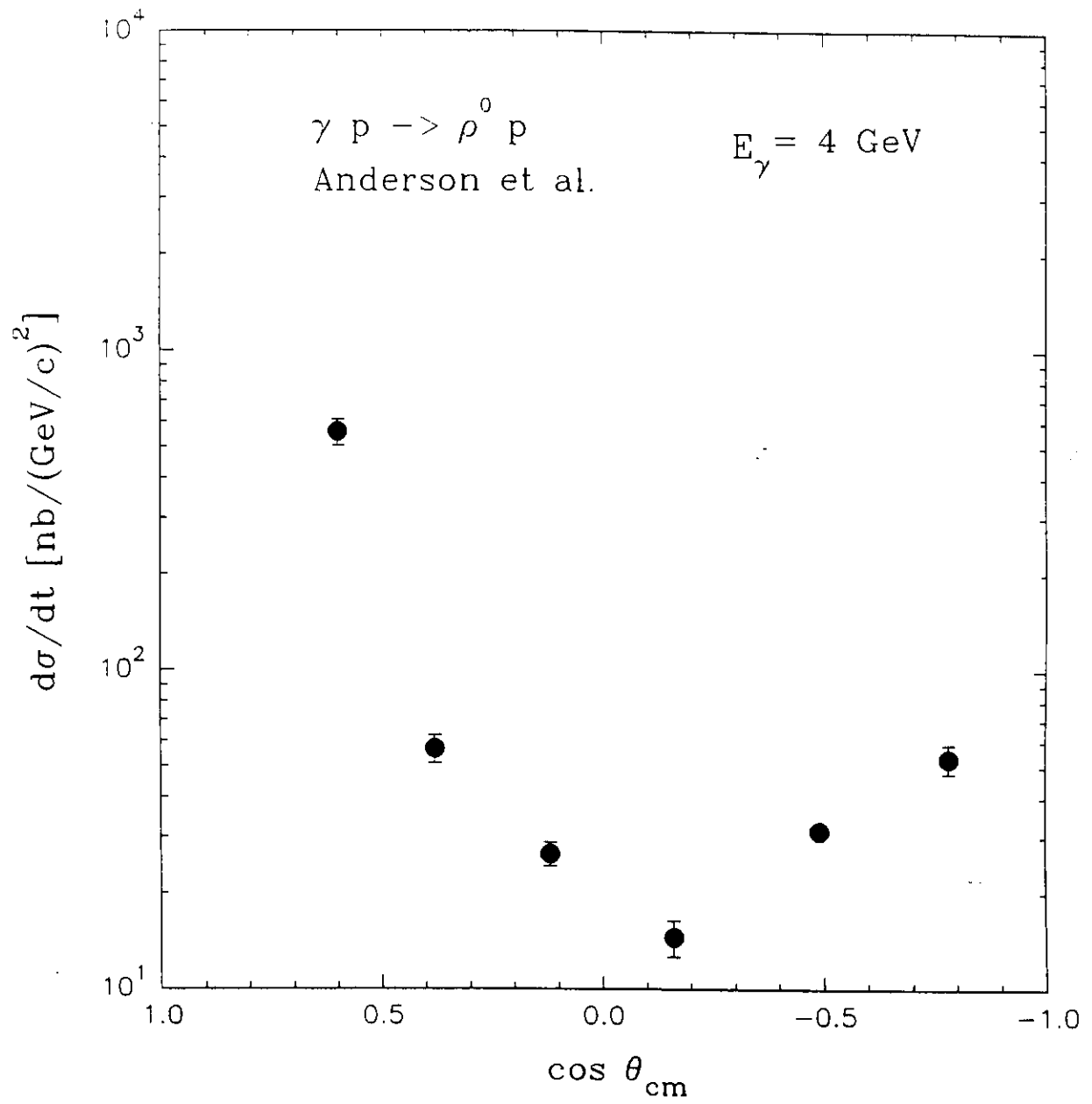


Figure 7: Data from Anderson *et al.* [19] at  $E_\gamma = 4.0 \text{ GeV}$  for  $\gamma p \rightarrow \rho^0 p$ .

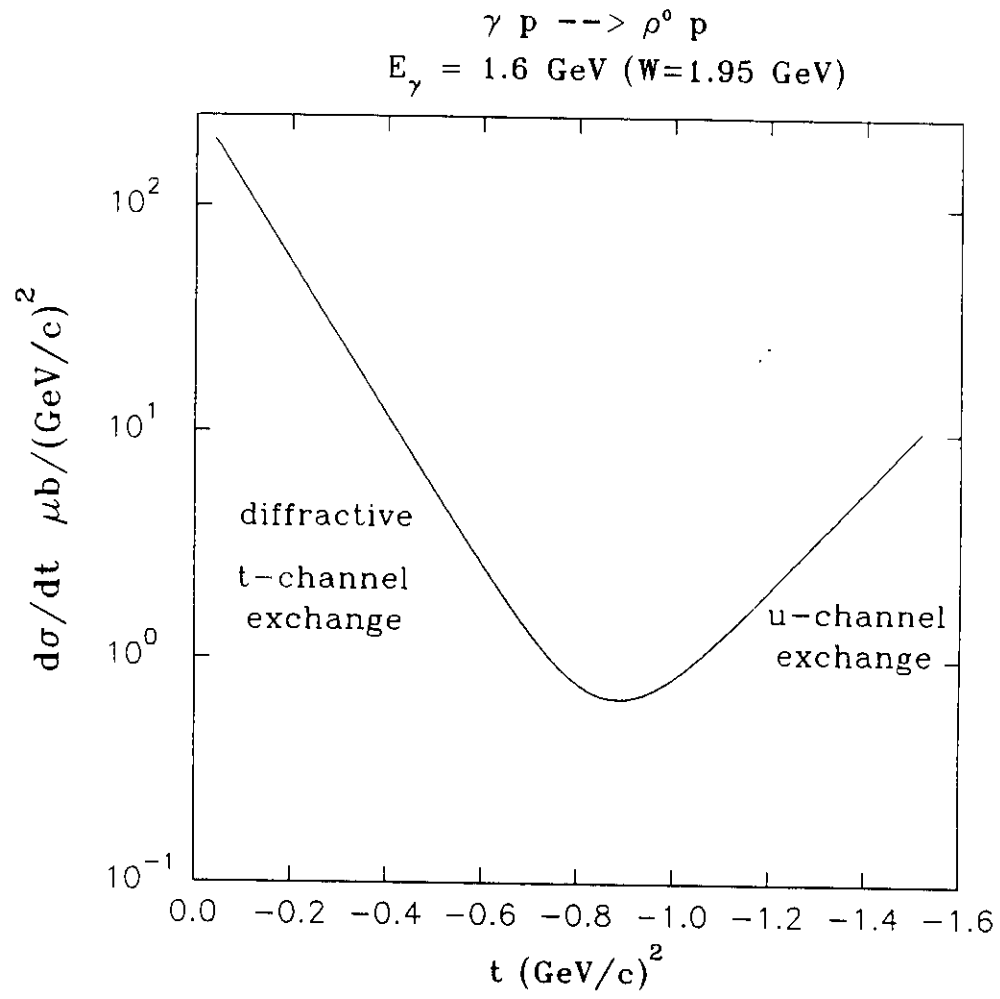


Figure 8: Extrapolation from high energy data [19] ( $E_\gamma = 4 \text{ GeV}$  assuming  $\sigma \sim s^{-7}$  down to  $E_\gamma = 1.6 \text{ GeV}$ ).

Table 3: Summary of pertinent measurements with near or overlapping kinematics.

Author	Reaction	$E_\gamma$ (GeV)	$ t $ (GeV/c) <sup>2</sup>	Detector	Polarized?	Tagged?
Criegee [25]	$\bar{\gamma}p \rightarrow \rho^0 p$	1.4 – 3.3	$< 0.4$	telescopes	yes <sup>a</sup>	no
Ballam [12]	$\bar{\gamma}p \rightarrow \rho^0 p$	2.8, 4.7	$< 1.0$	bubble chamber	yes <sup>b</sup>	no
Anderson [20]	$\gamma p \rightarrow \rho^0 p$	5.0 – 17.8	$< 1.1$	p spectrometer	no	no
Clift [21]	$\gamma p \rightarrow \rho^0 p$	3.5	$ u  < 1.4$	p spectrometer	no	yes
Anderson [19]	$\gamma p \rightarrow \rho^0 p$	4.0	$< 5.0$	counters, spectrometer	no	no
Benz [26]	$\gamma d \rightarrow \rho^0 d$	1.8 – 2.5	$< 0.2$	bubble chamber	no	no
ABBHHM [22]	$\gamma p \rightarrow \rho^0 p$	1.4 – 1.8	$< 1.3$	bubble chamber	no	no
Erbe [23]	$\gamma p \rightarrow \rho^0 p$	1.4 – 1.9	$< 1.0$	bubble chamber	no	no
Davier [27]	$\gamma p \rightarrow \rho^0 p$	2.0 – 4.0	$< 0.45$	streamer chamber	no	no
Barber [28]	$\gamma p \rightarrow \rho^+ n$	2.8 – 3.5	$< 0.3$	spectrometer	no	yes
Hilpert [24]	$\gamma d \rightarrow \rho^- pp_s$	1.4 – 2.5	$< 1.1$	bubble chamber	no	no
Benz [26]	$\gamma d \rightarrow \rho^- pp_s$	1.2 – 2.5	$< 1.0$	bubble chamber	no	no

<sup>a</sup>Coherent bremsstrahlung

<sup>b</sup>Compton backscattering

background compared with that for the  $\gamma p \rightarrow \rho^0 p$  reaction.

There are many fewer data for charged  $\rho$  photoproduction than for  $\rho^0$  photoproduction; and *no experiments at all have been performed with linearly polarized photons*. A search for resonance production decaying via a charged  $\rho$  has been studied only for  $\gamma n \rightarrow \rho^- p$  [24]. The cross section (for  $1.4 < E_\gamma < 2.5$  GeV) is not at all described by a purely one-pion-exchange mechanism, and has a plateau above  $|t| = 1.0$  (GeV/c)<sup>2</sup>, as shown in Fig. 9. A large enhancement of the cross section, plotted as a function of photon energy (Fig. 10) is seen in the range  $1.5 < E_\gamma < 2.2$  GeV. This is precisely the region where resonance effects should be the greatest. We expect the cross section for  $\gamma p \rightarrow \rho^+ p$  to be similar to the  $\rho^-$  photoproduction cross section.

A summary of previous measurements that overlap the kinematics we wish to explore is contained in Table 3.

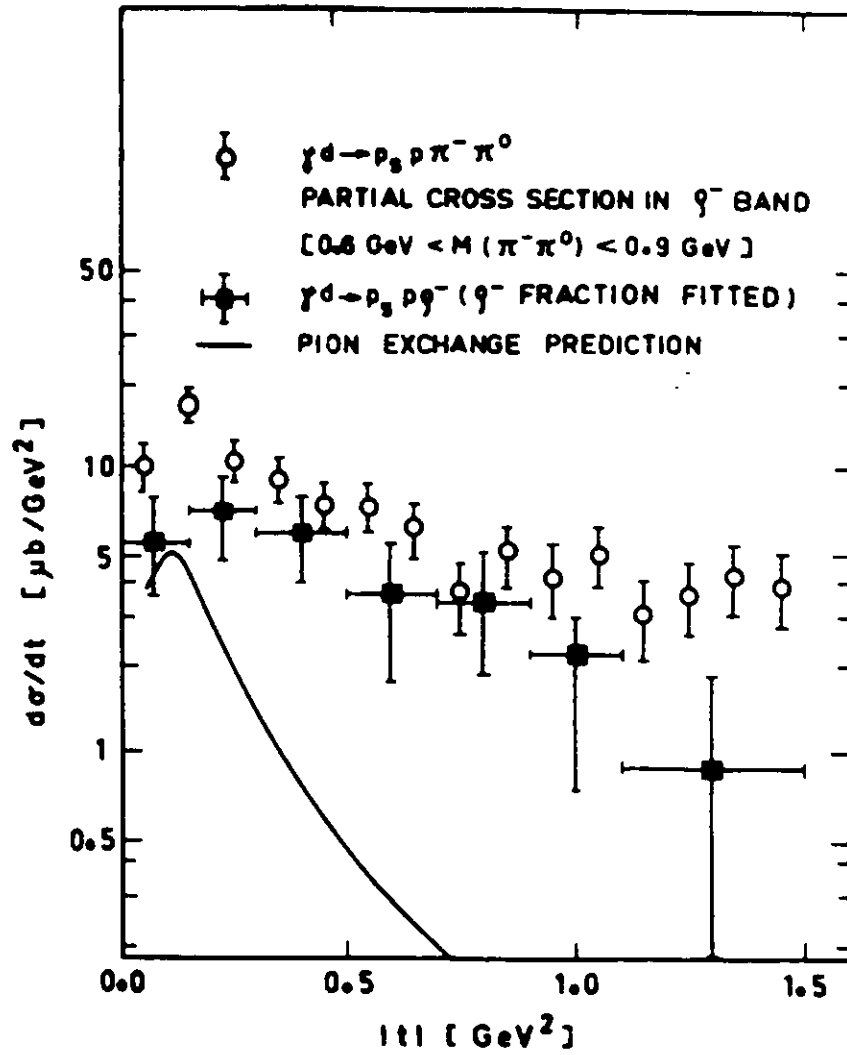


Figure 9: Data from Hilpert *et al.* [24] showing  $d\sigma/dt$  for  $1.4 < E_\gamma < 2.5$  GeV for the reaction  $\gamma d \rightarrow \rho^- p p_s$ , where  $p_s$  is a spectator proton.

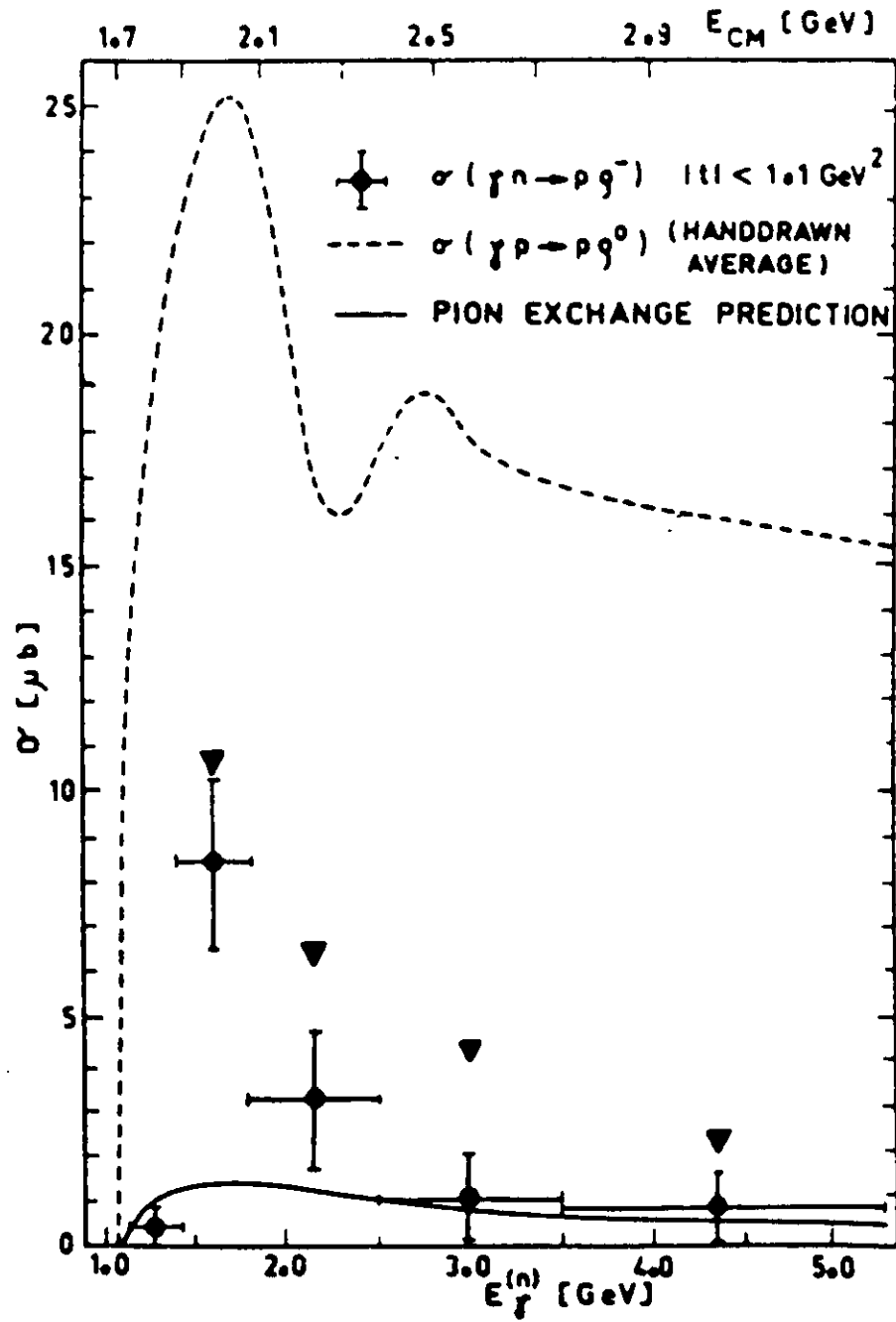


Figure 10: Data from Hilpert *et al.* [24] showing  $\sigma$  for  $-t < 1.1 \text{ (GeV/c)}^2$  for the reaction  $\gamma d \rightarrow \rho^- p p_s$ , where  $p_s$  is a spectator proton.

## 4 Acceptances

Extensive background and acceptance studies have been carried out for the  $p(\gamma, p\pi^+)\pi^-$  and  $p(\gamma, n\pi^+\pi^0)$  reactions. The details of these studies are given in Appendix A. Here, we will summarize the principal results, namely (a) the techniques that we have developed in distinguishing the reaction  $\gamma p \rightarrow \rho^0 p$  from either the primary two-pion ( $\gamma p \rightarrow \Delta\pi$ ) or three-pion ( $\gamma p \rightarrow \omega p$ ) backgrounds, and (b) how we extract the underlying density matrix elements that characterize the  $\pi^+$  angular distributions.

The primary difficulty in identifying the photoproduced  $\rho^0 p$  channel is in efficiently separating  $\rho$ -meson and non- $\rho$ -meson events without unduly sacrificing the acceptance. The events were generated uniformly in phase space, Lorentz boosted to the laboratory frame, and fed into the CLAS simulation program FASTMC. We generated 50,000 events for both our signal ( $\rho^0 p$ ) and our background ( $\Delta\pi$  and  $\omega p$ ) studies. A  $p$ - $\pi^+$  coincidence defines the minimum condition for an accepted event. The overall acceptance for  $p(\gamma, p\pi^+)X$  is approximately 50% (40%) for the two-pion (three-pion) channel for the incident photon energy range of  $1.3 < E_\gamma < 2.1$  GeV, and is almost independent of magnetic field strength for positive polarities. We have developed powerful software cuts (see section A.3) which enable us to identify the  $\rho^0 p$  channel. In Fig. 11, we overlay the acceptance distributions,  $\varepsilon = \varepsilon(t)$ , of the signal and the sum of the background channels, for the incident photon energy  $E_\gamma = 1.7$  GeV, after all cuts have been imposed. We make the following assumptions (see section A.5)

$$\begin{aligned} \frac{\sigma(\gamma p \rightarrow \rho^0 p)}{\sigma(\gamma p \rightarrow \Delta^{++}\pi^-)} &= 2 \\ \frac{\sigma(\gamma p \rightarrow \rho^0 p)}{\sigma(\gamma p \rightarrow \omega p)} &= 3 \\ \frac{\sigma(\gamma p \rightarrow \Delta^{++}\pi^-)}{\sigma(\gamma p \rightarrow \Delta^0\pi^+)} &= 3 \end{aligned}$$

We see that in the central  $t$  region, the ratio of the signal to integrated background is 9:1. In Fig. 12, we plot the overall acceptance as a function of incident photon energy for the reaction  $\gamma p \rightarrow \rho^0 p$ . We next employed the program GEN\_MATRIX\_EVENTS [29] to generate the events in accordance with the differential cross section  $W(\cos\theta, \phi, \Phi)$ . As has been already noted in eq. 1, this quantity can be expressed in terms of the spin density



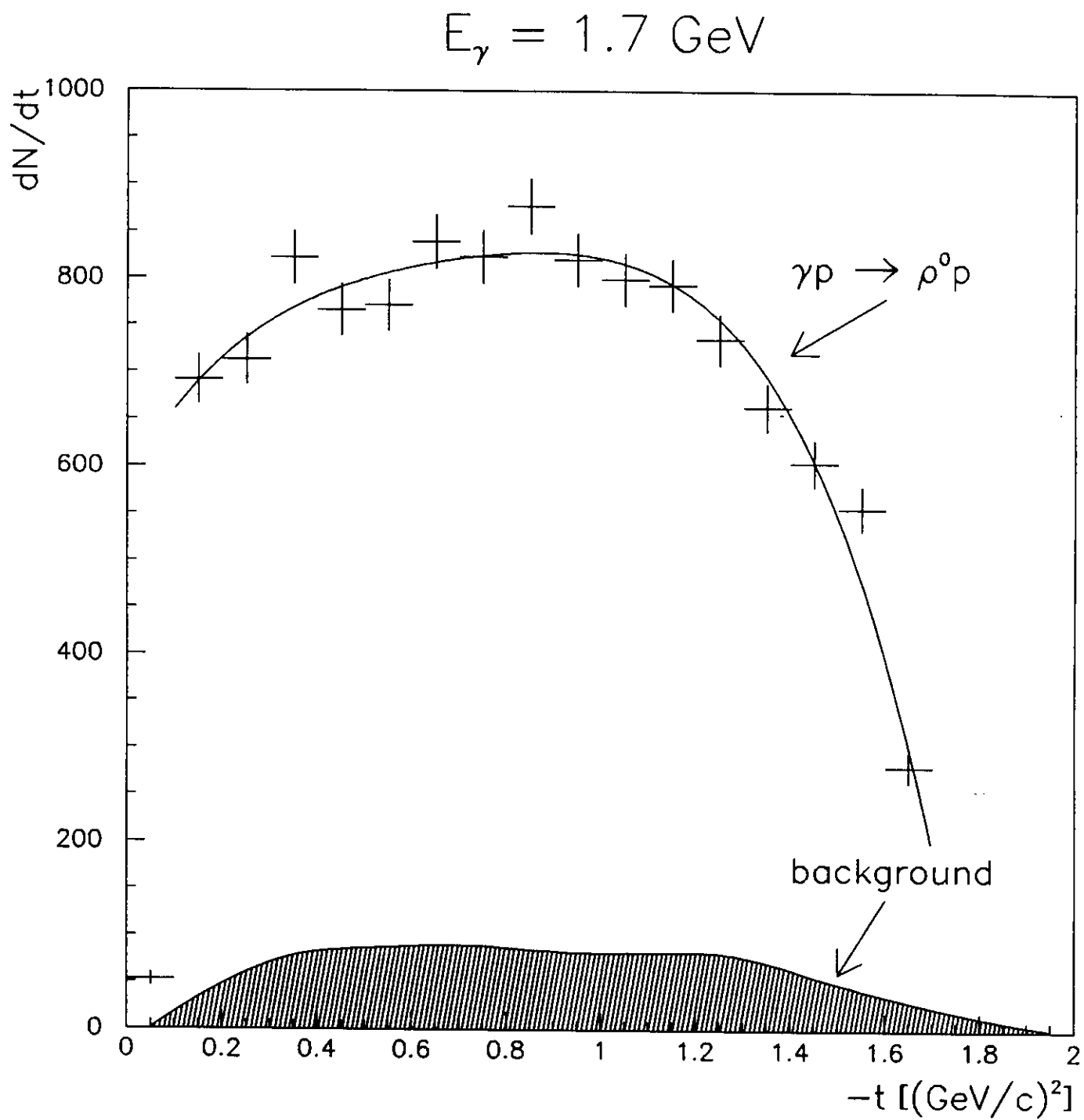


Figure 11: Overlay of the acceptance for the signal ( $\rho^0 p$ ) and the sum of background ( $\Delta^{++}\pi^-$ ,  $\Delta^0\pi^+$ , and  $\omega p$ ) channels, after all software cuts have been applied, for  $E_\gamma = 1.7 \text{ GeV}$ .

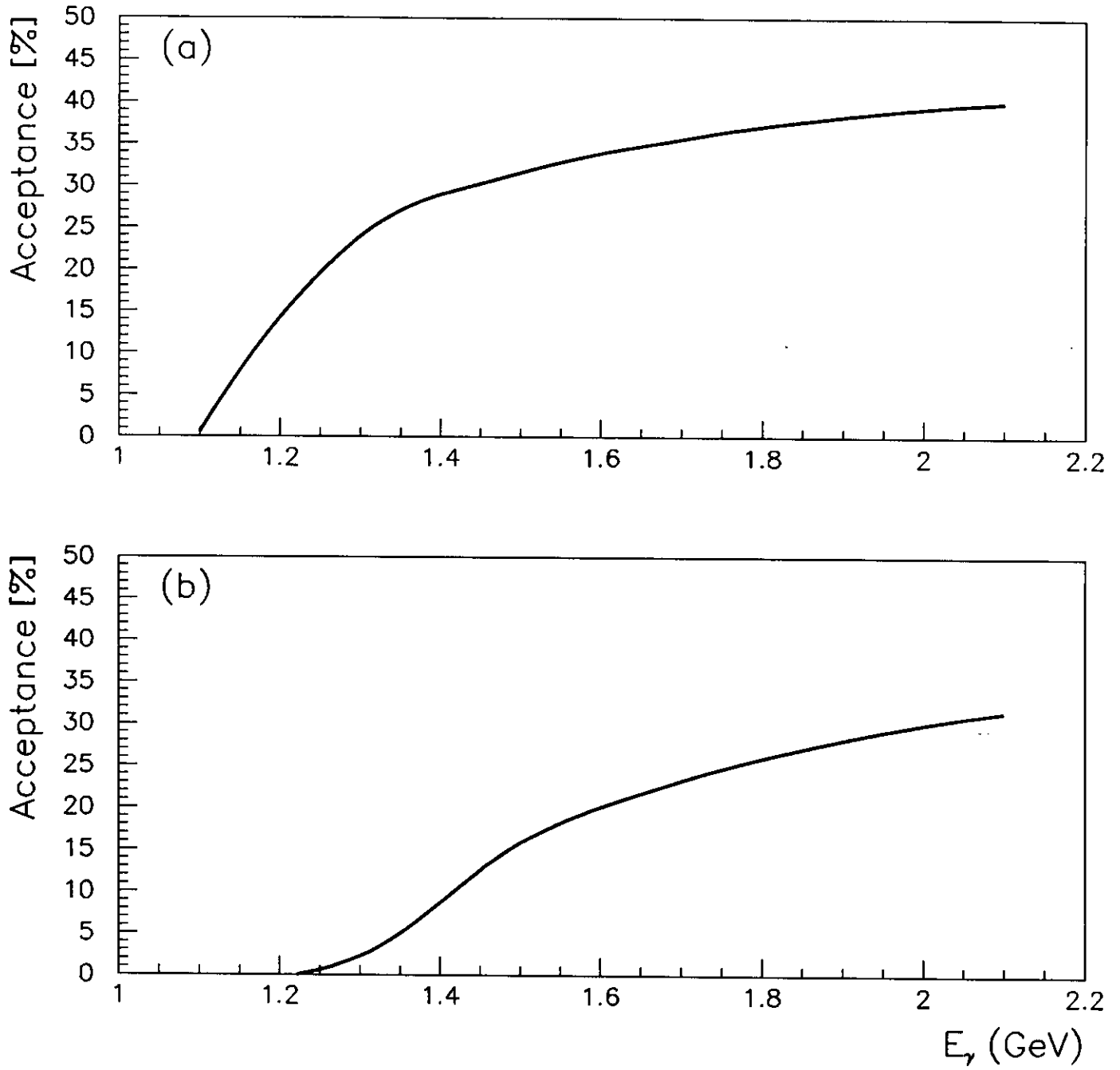


Figure 12: The overall acceptance is plotted as a function of the incident photon energy for  $B = +B_0$  after application of (a) the  $\Delta^{++}$  cut and (b) the  $\Delta^{++}$  and  $\Delta^0$  cuts.

matrix elements  $\rho_{\alpha\beta}^n$ . These multiplicative factors govern the angular distribution of the two-pion decay of the  $\rho$  meson. We refer the reader to section A.6, in which the mathematical details for the extraction of the density matrix elements is discussed thoroughly. Here, we simply present the results for the unpolarized case. Preliminary results for the polarized case are presented in section A.6. From the input density matrix elements provided by Roberts, we generated the pion distribution in accordance to  $W(\cos\theta, \phi, \Phi)$ . After making all the necessary Lorentz boosts (both from and to the helicity and laboratory frames), the particles were fed into the detector simulation program, processed and analyzed, and then the output density matrix elements were extracted. In Fig. 13, we superimpose the input (dashed line) and the output (inverted triangles) density matrix elements. We observe that the output values agree remarkably well with the input. To our knowledge, we are the first group to have successfully retrieved density matrix elements using simulated data, with proper error propagation, that take the CLAS acceptance into account.

(Unpolarized)  $\sqrt{s} = 1.95$  GeV

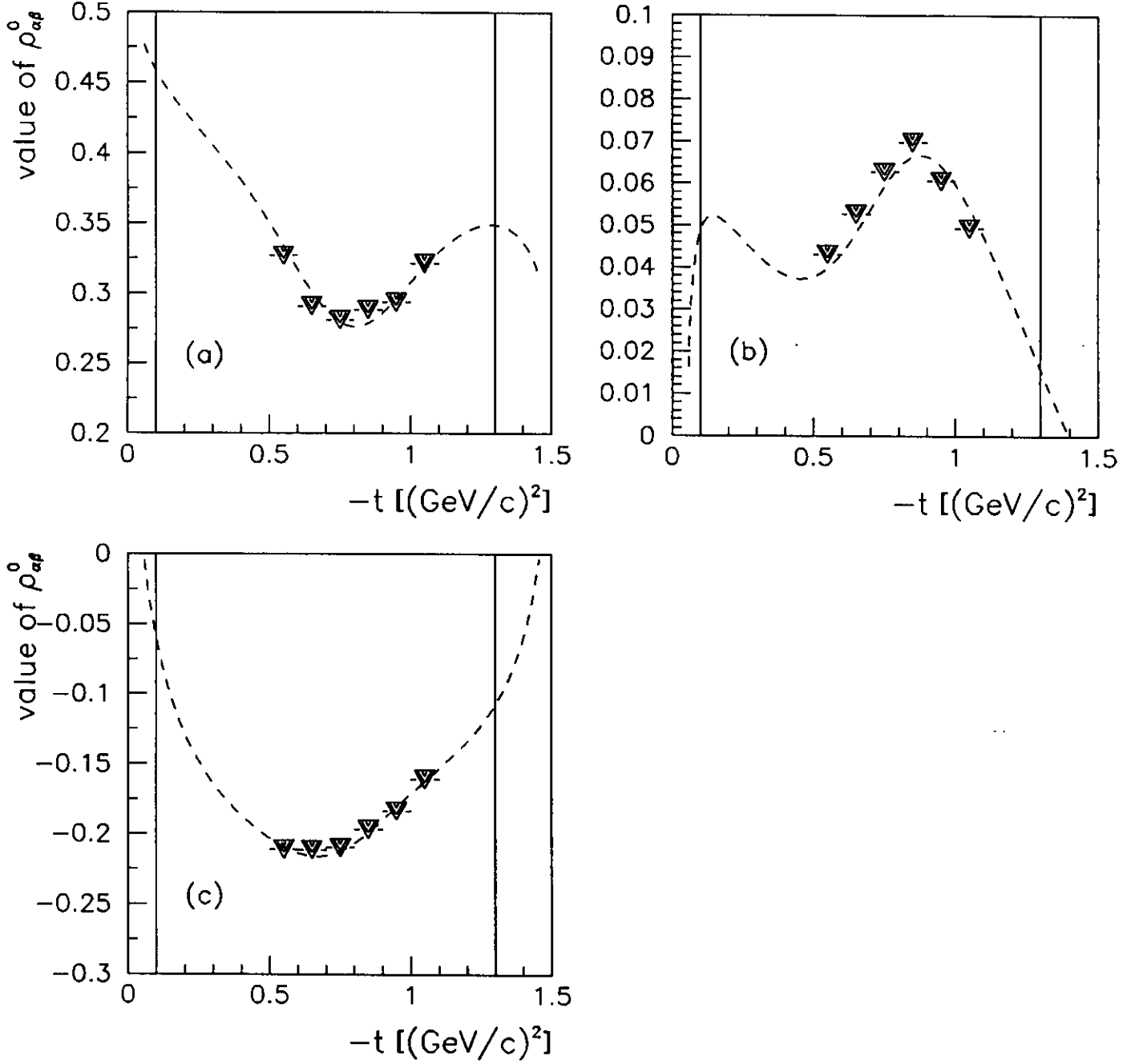


Figure 13: Retrieved density matrix elements after processing events through FastMC, superimposed on the input curves for (a)  $\rho_{00}^0$ ; (b)  $\text{Re}\rho_{10}^0$ ; and (c)  $\rho_{1-1}^0$ . The vertical lines denote the region of acceptance.

## 5 Experimental Parameters

### 5.1 Linearly Polarized Photons

Two methods of producing linearly polarized photons in Hall B have been considered. We propose to use a coherent bremsstrahlung beam. Our collaboration intends to design and implement such a coherent bremsstrahlung capability in Hall B. One can obtain significant linear polarizations through the use of a crystal radiator (diamond). The use of Compton backscattering from a laser [30] will produce a high quality photon beam with high polarization and low systematic errors; however, even by using the frequency doubling technique, the highest photon energy attainable (1.8 GeV with a 6 GeV electron beam) will only partially cover our region of interest. We will use the Compton source if it is available when this experiment is scheduled to run, for that part of the experiment for  $E_\gamma \leq 1.8$  GeV, if it produces improved results for the same amount of beamtime.

The method of coherent bremsstrahlung has been used at SLAC, Mainz, and other facilities. For a detailed description of the theory see Ref. [31], [32]. The apparatus necessary to implement this capability is relatively straightforward: a diamond crystal mounted on a goniometer placed near to the nominal radiator position. A much more detailed description of coherent bremsstrahlung is given in Appendix B.

### 5.2 Count Rate Estimates

We have performed a study [33] to determine the usable tagging rate with a coherent bremsstrahlung spectrum as given by Fig. 14, for both the 4 GeV and 6 GeV incident electron energy bites. As shown in the figure, the solid line corresponds to the 4 GeV incident electron coherent bremsstrahlung spectrum with the coherent peak at a maximum at 1.5 GeV. In the 6 GeV electron energy case (dashed line), the coherent peak is at a maximum at 2.1 GeV.

We assume the  $\text{LH}_2$  target to be of length 14 cm and that any  $\gamma + p$  event will cause a CLAS event with 80% probability, independent of energy or multiplicity. We assume that the event rate will be limited by a total trigger rate of 1 kHz. Data from Refs. [22] and [23] indicate that the nondiffractive cross section at this photon energy resulting from the reaction  $\gamma p \rightarrow \rho^0 p$  is  $d\sigma/dt \simeq 7 \mu\text{b}/(\text{GeV}/c)^2$  in the four-momentum transfer squared range of  $0.4 < -t < 1.0 (\text{GeV}/c)^2$ . The anticipated number of  $\rho^0$  events produced per second

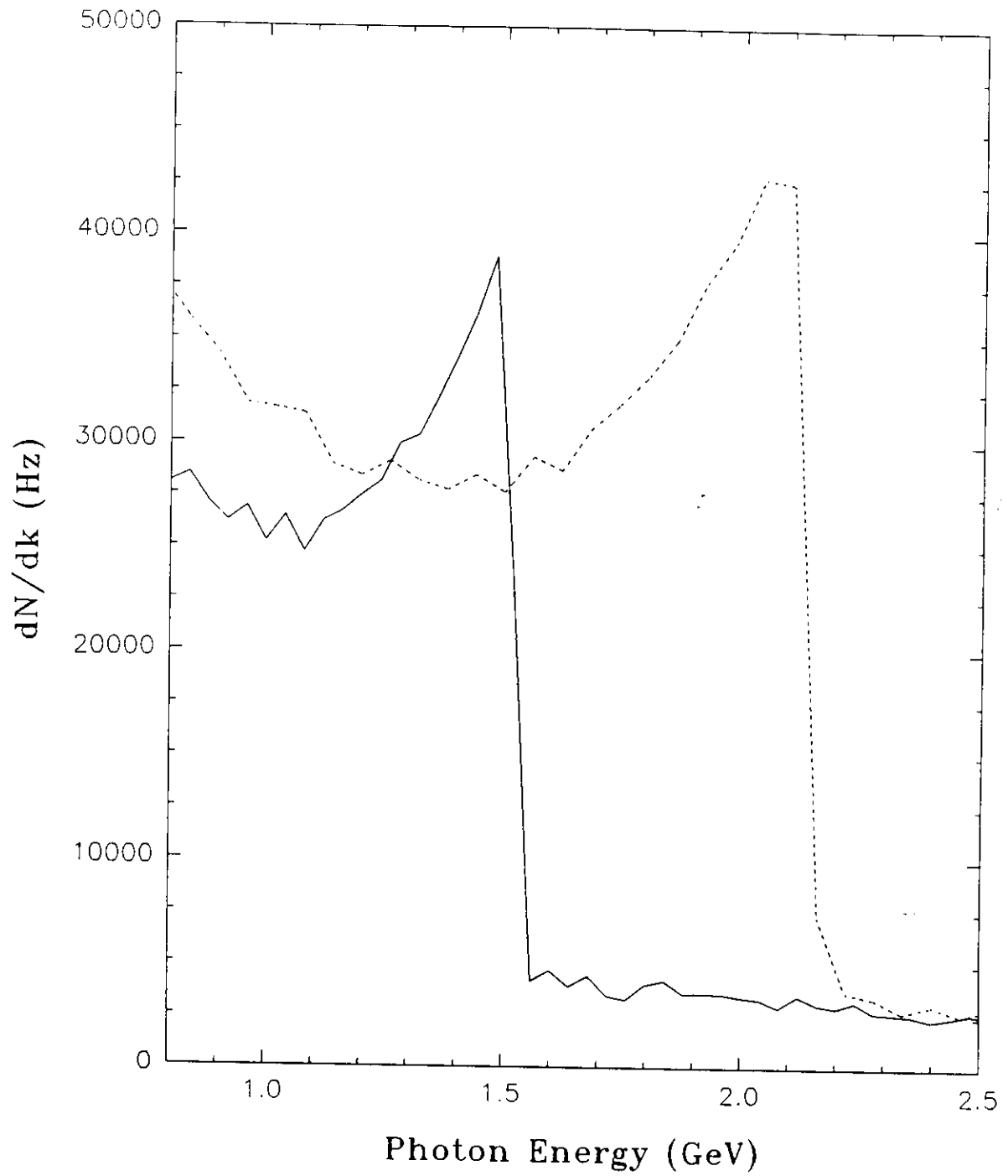


Figure 14: Simulation of coherent bremsstrahlung under Hall B conditions at  $E_0 = 4 \text{ GeV}$  (solid) and  $E_0 = 6 \text{ GeV}$  (dashed), for a  $10 \mu\text{m}$  diamond crystal radiator with no collimation.

Table 4: Summary of our count rate calculation. The number of events is calculated for the four-momentum transfer squared range of  $0.4 < -t < 1.0$  (GeV/c)<sup>2</sup>. The real to accidental rate is constrained to be 2:1.

$E_0$ [GeV]	Tagging Range [GeV]	Tagging Rate [Hz]	$N_{\text{evts}}$ [Hz]
4.0	0.8 – 1.6	$6.0 \times 10^6$	10.0
6.0	1.2 – 2.4	$4.5 \times 10^6$	7.5

within this  $t$  range is

$$N_{\text{evts}} = \frac{2}{3} \Phi N_{\text{nucl}} \frac{d\sigma}{dt} \Delta t$$

where the factor  $\frac{2}{3}$  is the ratio of real events to (real events + accidentals),  $\Phi$  is the photon rate,  $N_{\text{nucl}} = N_A \rho \tau$ ,  $\rho \tau$  is equal to  $(0.071 \text{ g/cm}^3)(14 \text{ cm})$ , and  $\Delta t$  has been set to  $0.6 \text{ (GeV/c)}^2$ . A summary of the results is given in Table 4.

We will bin the data in bins of 50 MeV width in  $\sqrt{s}$  and  $5^\circ$  in  $\theta_{\text{cm}}$ . The c.m. energy spans approximately 560 MeV for our range in photon energies. Based upon our CLAS acceptance studies, we will measure the c.m. polar angular region from  $\theta_{\text{cm}} = 35^\circ$  to  $\theta_{\text{cm}} = 145^\circ$ ; we expect the resonance photoproduction is most pronounced in the region between  $\theta_{\text{cm}} < 65^\circ$  and  $\theta_{\text{cm}} > 115^\circ$ . Because the count rate outside the central  $\theta_{\text{cm}}$  region is 5 to 10 times greater, we will have sufficient statistics to extract the density matrix elements over  $|\cos \theta_{\text{cm}}| < 0.8$  and hence over a wide range in  $t$ .

We will therefore have 242 bins in all: 11 bins in  $\Delta\sqrt{s}$  and 22 bins in  $\Delta\theta_{\text{cm}}$ . Folding in our efficiency in reconstructing  $N^*$  events, we will need at least 100 000 events generated per each bin, near  $\theta_{\text{cm}} = 90^\circ$ , in  $\Delta\sqrt{s}\Delta\theta_{\text{cm}}$  to ensure meaningful reconstruction of the angular distributions of the pions in the helicity frame. In Figs. 15 and 16 we plot the model predictions of Roberts. The error bars reflect the anticipated experimental uncertainties of 5%.

### 5.3 Beamtime Request

We are requesting two separate data-taking runs; one with a 4 GeV electron beam with the coherent peak tuned to a maximum polarization at 1.5 GeV and another measurement with

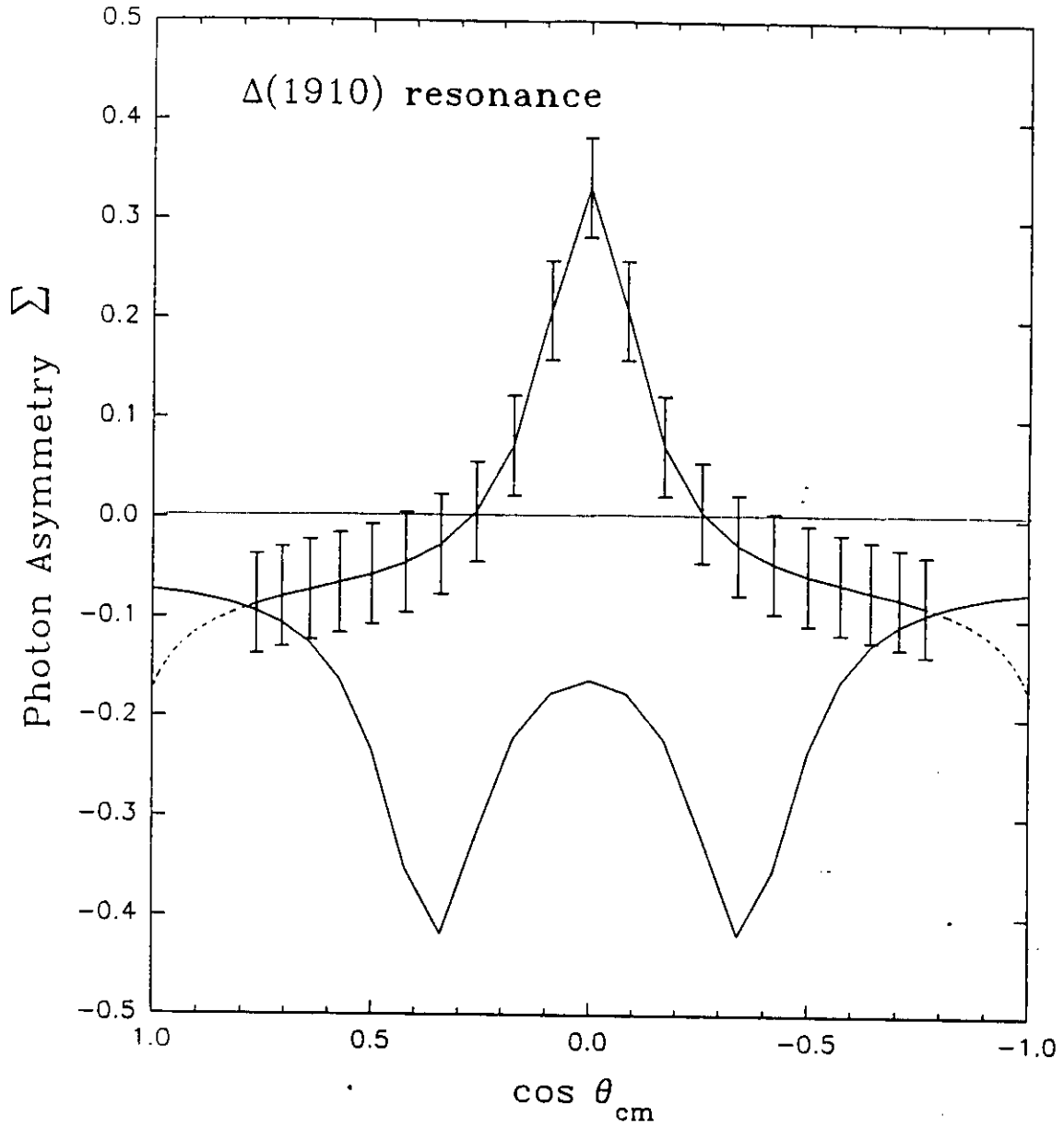


Figure 15: The photon asymmetry  $\Sigma$  for the  $N_{\frac{3}{2}}^{+}(1910)$  calculated by Roberts [14]. The two curves are for the same asymmetry but with a sign change in the dominant partial wave amplitude. The data represent expected binning from this experiment and expected uncertainties.



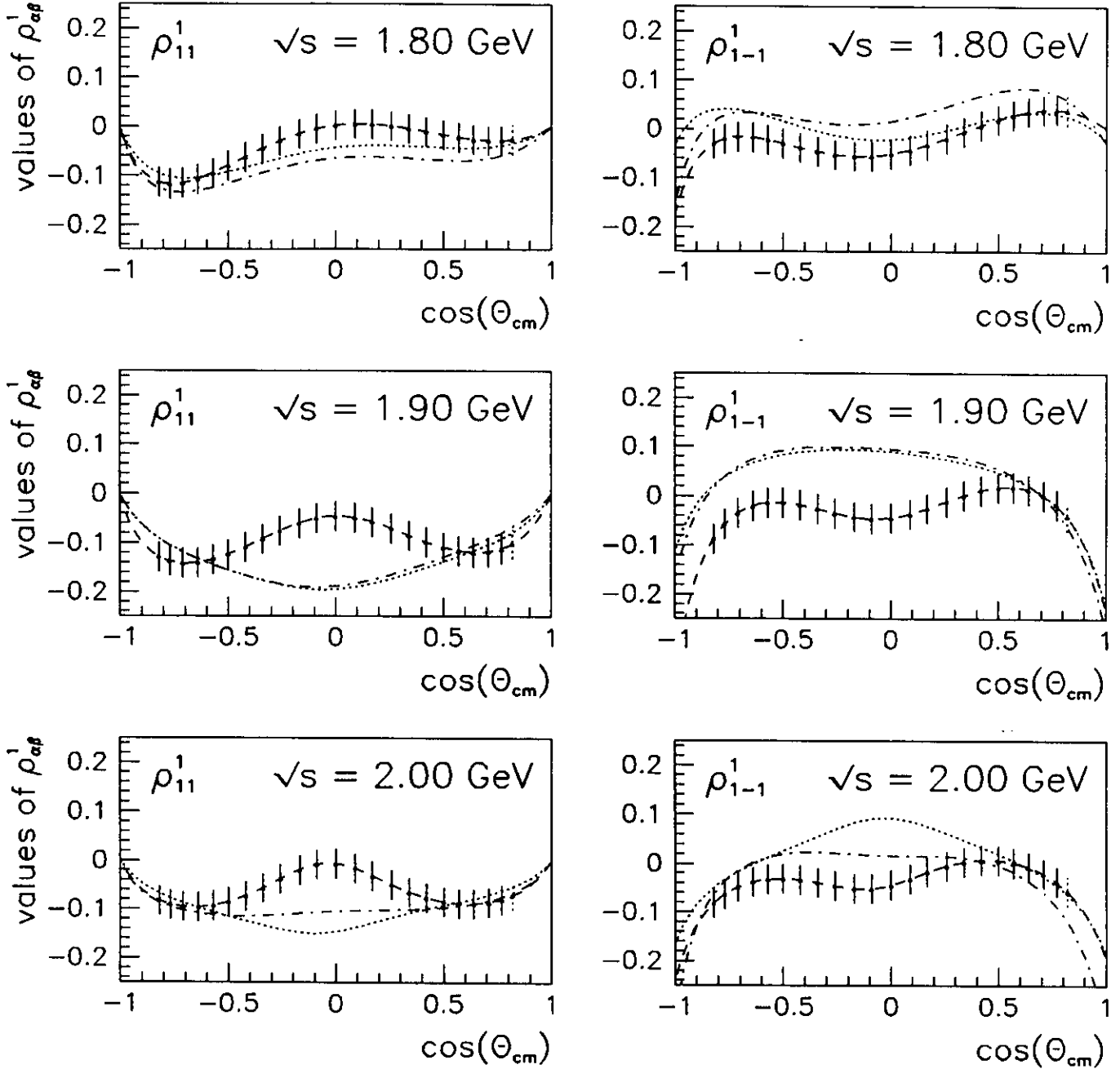


Figure 16: Predictions of the theory by Roberts [14]: (dashed line) only one missing resonance included; (dashed-dotted line) all but one of the missing resonances included; and (dotted line) all missing resonances included. The data represent expected binning from this experiment and expected uncertainties.

a 6 GeV beam with the maximum polarization of the coherent peak situated at 2.1 GeV. Figure 17 shows the calculated beam polarizations expected as a function of photon energy for both 4 GeV and 6 GeV electron energies. Since the widths of most baryon resonances are of the order of 150 MeV, it is necessary to obtain data over a broad range in c.m. energy. With the coherent peaks chosen as in Fig. 17, we will cover a range from below the nominal threshold for  $\rho$  photoproduction to an energy somewhat above the region where the missing resonances have been predicted.

We have looked at the option of using a 4 GeV beam for both energy bites. Two points must be kept in mind: the statistical uncertainty is proportional to the inverse of the square of the beam polarization, and the polarization for a given electron energy decreases as the coherent peak is shifted to higher photon energy. This second point is demonstrated in Fig. 18, which compares the photon polarization from 4 and 6 GeV electron beams with the peak polarization occurring at 2.1 GeV. In the region between 1.5 and 2.1 GeV, the average polarization from the 4 GeV beam ( $\sim 35\%$ ) is half that of the 6 GeV beam ( $\sim 70\%$ ), meaning that we would have to run four times longer at 4 GeV to attain the same degree of precision in our measurements.

The difference in polarization between 4 and 6 GeV incident electrons is much smaller for the lower energy bite, as shown in Fig. 19. The 10% reduction in polarization for the 4 GeV case means that we require two more days, in addition to the nine days needed to perform the experiment with a 6 GeV beam, to attain the accuracy quoted above.

We request 20 days to run this experiment. We require incident electron energies of 4 and 6 GeV and the CLAS magnetic field set to positive polarity and full strength. We will run at least one day for each energy with the photon polarization direction shifted by  $90^\circ$  in order to understand the azimuthal systematics of the CLAS detector. Our beamtime request does not include setup time for the coherent bremsstrahlung facility; we estimate that this can be accomplished in three days of beamtime. Our beamtime request for experimental running is

**1st run:      11 days with  $E_0 = 4$  GeV**

**2nd run:      9 days with  $E_0 = 6$  GeV**

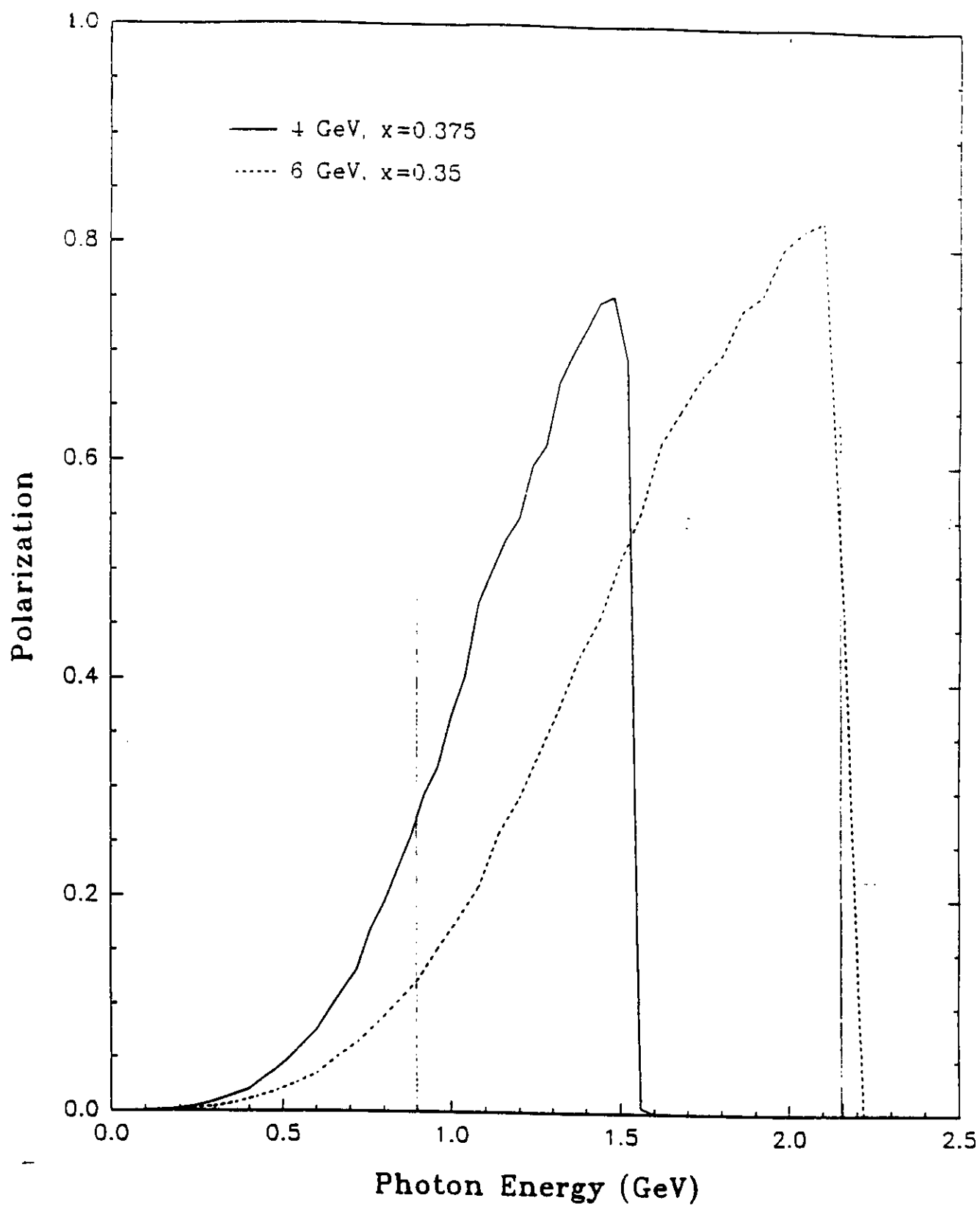


Figure 17: Polarization spectrum for both the 4 GeV (dashed line) and 6 GeV (solid line) portions of the experiment. We are interested in measuring the region from 1.0 GeV to 2.2 GeV.

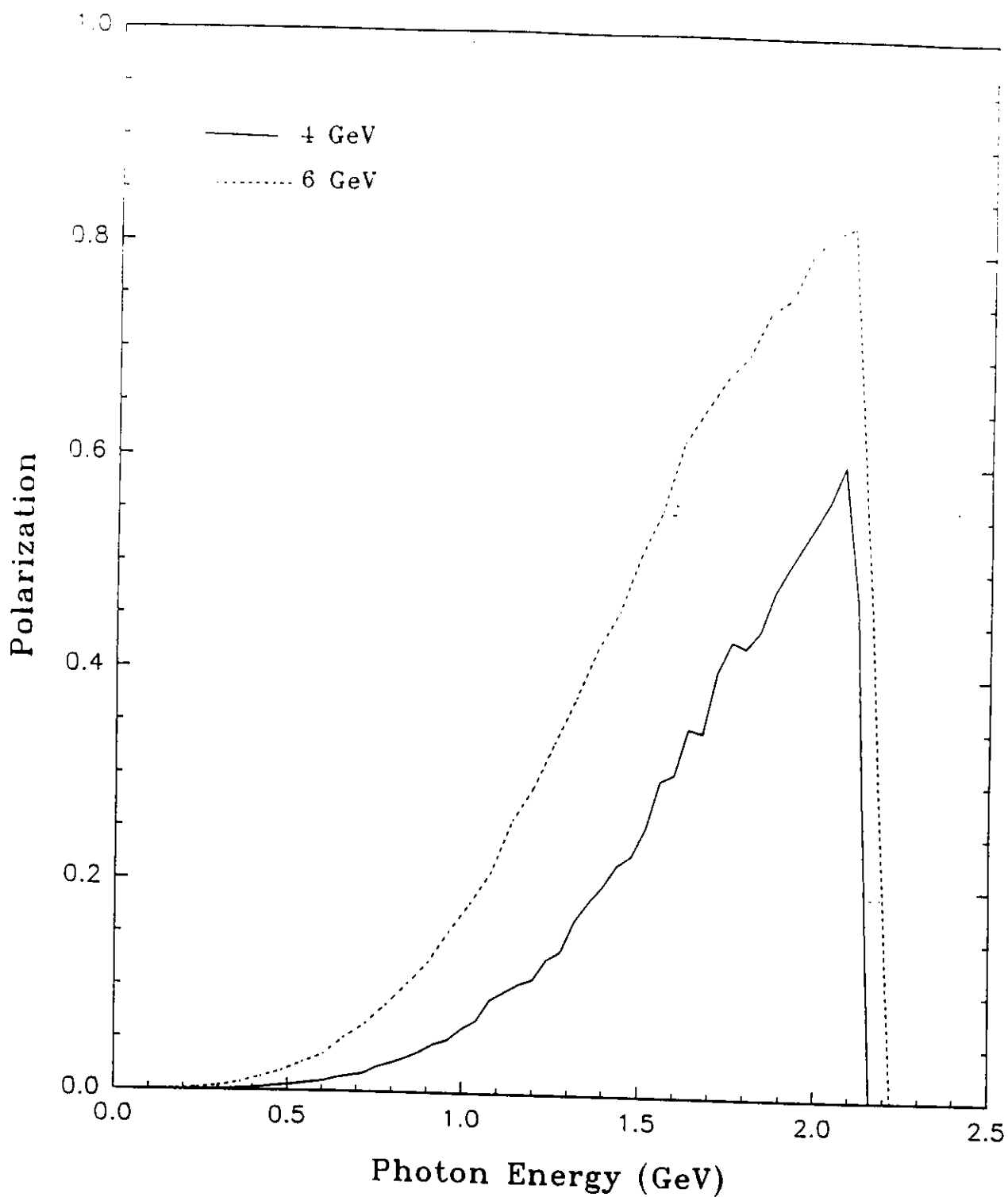


Figure 18: Polarization spectrum showing both 4 GeV and 6 GeV incident electron energies. Both coherent peaks were computed for maximum polarizations at a photon energy of 2.1 GeV.

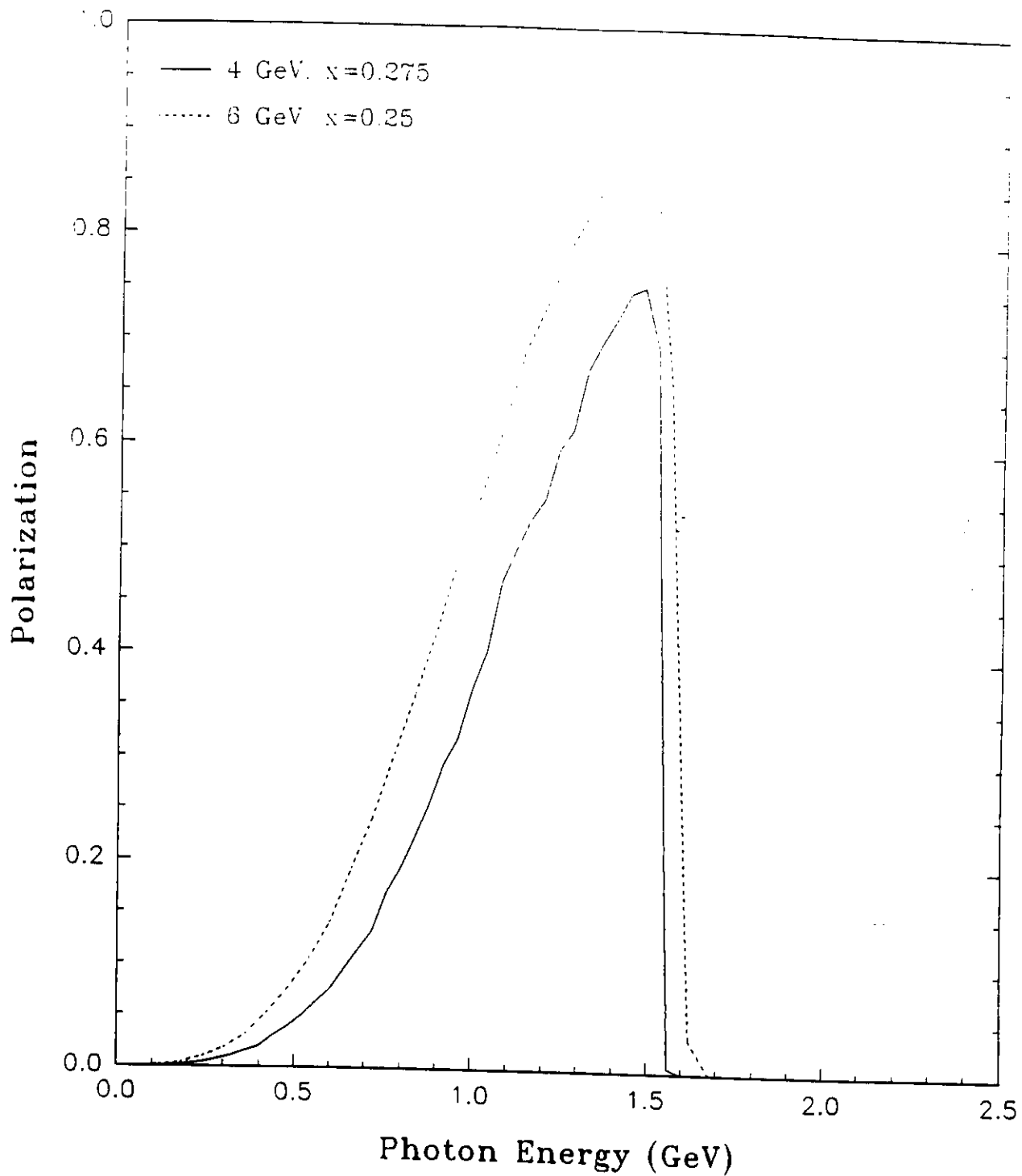


Figure 19: Polarization spectrum showing both 4 GeV and 6 GeV incident electron energies. Both coherent peaks were computed for maximum polarization at a photon energy of 1.5 GeV.

## 6 Further Experiments

We plan on running with a minimum bias trigger, requiring that only one charged particle be detected in the CLAS. This will allow other possible experiments, such as

$$\vec{\gamma}p \rightarrow \pi N$$

$$\vec{\gamma}p \rightarrow \gamma p$$

$$\vec{\gamma}p \rightarrow \phi p$$

$$\vec{\gamma}p \rightarrow \omega p$$

to run concurrently with this experiment. This group anticipates participating in future proposals addressing the physics of these experiments.

## A Acceptance Studies

In this Appendix, we discuss our studies of the geometrical acceptances for photoproduced  $\rho$  mesons resulting from  $\gamma p$  reactions in the CLAS detector. This study was undertaken to determine the feasibility of measuring the helicity frame polar and azimuthal angular distributions of the decay  $\pi^+$  as a function of  $t$  and  $\sqrt{s}$ . In the following subsections we will demonstrate that our cuts will eliminate 90% of the background, and that we can retrieve the underlying density matrix elements that characterize the  $\pi^+$  angular distributions. To our knowledge, we are the first group to have successfully retrieved density matrix elements using simulated data, with proper error propagation, that take the CLAS acceptance into account.

### A.1 Event Generator and Detector Simulation

We used the program GEN\_MATRIX\_ELEMENTS [29] to generate the events. We observe that the differential cross section is proportional to  $W(\cos\theta, \phi, \Phi)$ . As already noted in eq. 1, this quantity can be expressed in terms of the density matrix elements  $\rho_{\alpha\beta}^n$ . These multiplicative factors govern the angular distribution of the two-pion decay of the  $\rho$  meson.

The density matrix elements derived by Roberts [14] are a function of  $\sqrt{s}$  and  $t$ . The angular distributions of the pions are first calculated, and the event generator determines the probability density of the helicity frame polar,  $\theta_H$ , and azimuthal,  $\phi_H$ , angles of the pions for each  $t$  at a given  $\sqrt{s}$ . The helicity frame  $\pi^+$  polar and azimuthal angles are then sampled in accordance to the probability density function  $W(\cos\theta, \phi, \Phi)$ . In the helicity frame, which is also the rest frame of the  $\rho^0$ , the 3-momentum of the  $\pi^-$  is equal and opposite to the 3-momentum of the  $\pi^+$ . From these decay pions, we then calculate the four momentum of the  $\rho^0$  in the c.m. frame of the incident tagged photon and the target proton. The 3-momentum of the final-state proton is necessarily opposite to that of the vector meson in this frame of reference. We now have complete information about the four momenta of the three final-state particles (i.e.,  $\pi^+$ ,  $\pi^-$  and the proton). The pions are boosted to the lab frame in the direction opposite the  $z$  component of the  $\rho^0$ , and the components of the 3-momentum are rotated from the helicity frame coordinate system to the lab frame via an Euler angle transformation. The proton is likewise Lorentz boosted from the incident c.m. frame to the lab frame and the final-state particles are written to an

Table 5: Input parameters for FASTMC.

Target radius	3.17 cm
Target length	14 cm
Target material	liquid hydrogen
Container thickness	0.543 cm
Container density	1.25 g/cm <sup>3</sup>
Radiation length of container	33.3 cm
Spot size of photon beam	1.0 cm (rms)
No vertexing	the tracking does not include the vertex as a constraint
Uncertainty in momentum	positional measurement uncertainty and multiple scattering terms included
B field	+B <sub>0</sub> , full field, positive particles bend out

output file for each event. These events, in turn, are fed into the CLAS detector simulation package, FASTMC\_GEN [34]. FASTMC\_GEN incorporates almost all of the routines of FASTMC [35], with the added feature of neutral-particle and photon detection. FASTMC is a parametric Monte Carlo code that renders a realistic representation of the geometry and mass composition of the CLAS detector. This Monte Carlo package includes such effects as particle decay, multiple scattering,  $dE/dX$  losses, detector efficiencies, and geometrical acceptances. The user may select several input parameters, which include strength and polarity of the toroidal magnetic field, rms width of the photon beam, and dimensions and type of target. The input parameters listed in Table 5 were based upon the Saclay target blueprints, and we have included the contributions from the carbon fiber beampipe and the beam bucket identifier scintillators [36] as well.

## A.2 Analysis and Acceptance

After the events have been processed through FASTMC\_GEN, we are in the position to study the acceptance as a function of our cuts. Our primary objective is to determine the angular



distributions of the decay pions in the helicity frame. By comparing the measured density matrix elements with the input values, we are able to determine how well we will be able to reconstruct the true angular distribution of the pions.

### A.2.1 Charged Particles

For a particle that is tracked through the three separate drift chambers, and deposits energy in a TOF counter, we can calculate its mass from the relativistic relationship,

$$m^2 = |\vec{p}|^2 \frac{1 - \beta^2}{\beta^2},$$

where

$$\beta = \frac{1}{c} \frac{\ell}{\Delta t}.$$

Here,  $\ell$  is the path length to the TOF counter and  $\Delta t$  is the particle's time of flight. For this study, we folded  $\Delta t$  with a gaussian  $\sigma_t$  of between 100 and 200 picoseconds, depending upon which counter was hit.

### A.2.2 Neutral Particles

FASTMC\_GEN uses the routine Neutral\_Smear to account for measurement uncertainty in reconstructing the 4-momentum of neutrals that are detected in the electromagnetic shower counters. We are primarily concerned with detecting neutrons or gammas; all other neutral particles will have long since decayed before reaching the electromagnetic shower counter. For further details see Ref. [34]. We note, furthermore, that photons and neutrons can readily be separated in the electromagnetic shower counters by their markedly different signals [37]. The uncertainty in the rms timing was set to 1 ns. In Fig. 20, the  $\beta$  distribution for the photons and neutrons resulting from the reaction  $\gamma + p \rightarrow \rho^+ + n$  are superimposed ( $E_\gamma = 1.7$  GeV and  $B/B_0 = +0.25$ ). We observe that the  $\beta$  distributions of the neutrons and photons are clearly distinguishable, and a  $\beta$ -cut of  $\beta = 0.85$  will suffice to separate the neutrons from the photons.

## A.3 Identification of the Neutral Rho Channel

In the reaction  $\gamma + p \rightarrow \rho^0 + p$ , there are three charged particles in the final state, i.e.,  $\pi^+$ ,  $\pi^-$ , and the proton. Below we enumerate the selection criteria:

$$E_\gamma = 1.7 \text{ GeV}$$

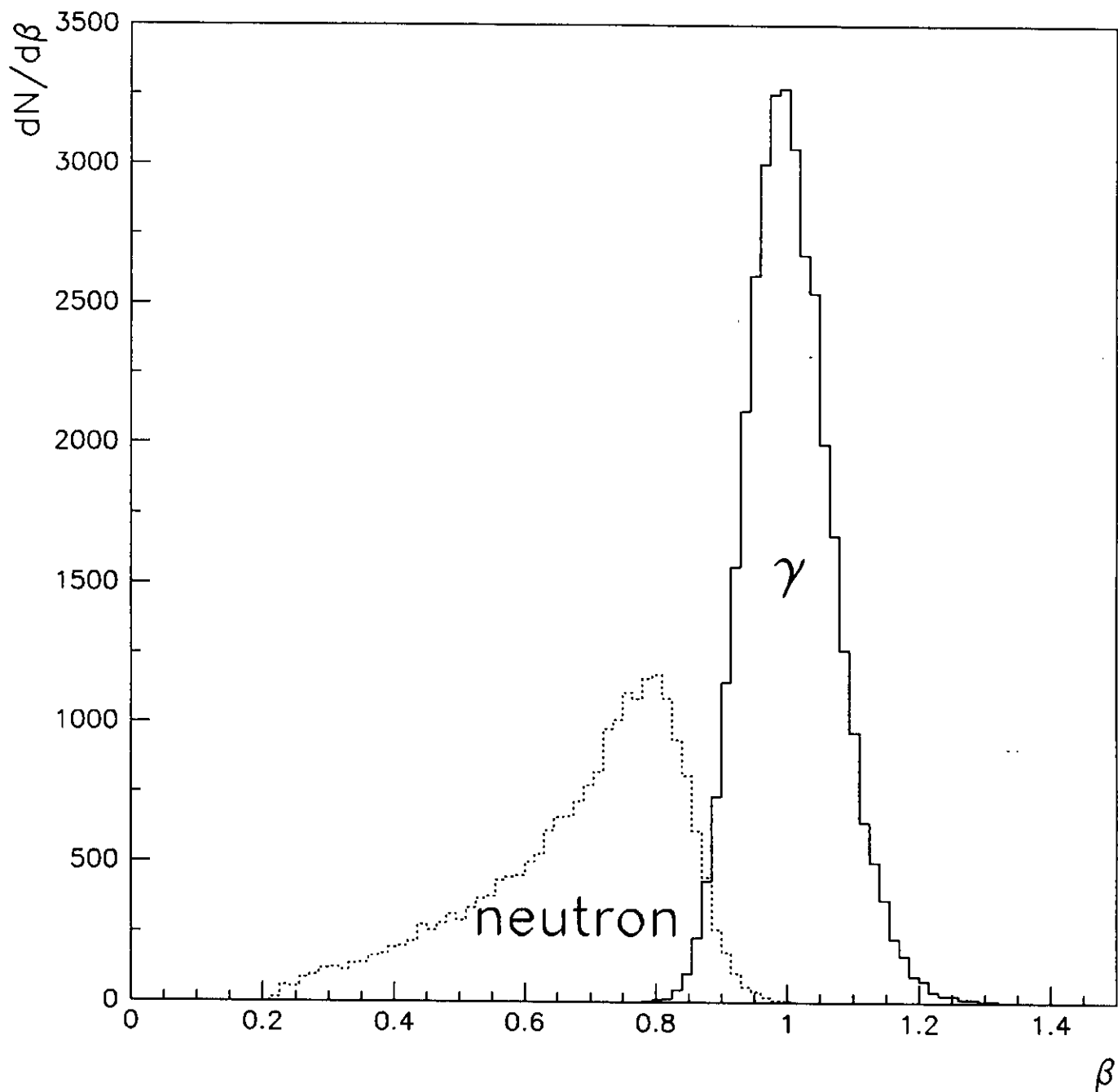


Figure 20: Beta distributions as measured by the electromagnetic counter for neutrons and decay photons arising from the reaction  $\gamma p \rightarrow \rho^+ n$ .

1. Only two positively charged particles in the final state. The particles are mass identified and the calculated masses are consistent with the masses of a proton and a  $\pi^+$ . That is to say, these particles are detected in the wire chambers, deposit energy in a TOF counter, and have reconstructed masses consistent with particle type, where

$$\begin{aligned}\pi: \quad & m^2 < 0.10 \text{ (GeV/c}^2\text{)}^2 \\ \text{proton:} \quad & m^2 > 0.65 \text{ (GeV/c}^2\text{)}^2\end{aligned}$$

2.  $\pi^-$  cut. If the missing mass squared,  $m_x^2$ , calculated from the four momenta of the proton and  $\pi^+$ , is within the range of  $-0.05 < m_x^2 < 0.09 \text{ (GeV/c}^2\text{)}^2$ , we keep the event

$$m_x^2 = (E_\gamma + m_{\text{tgt}} - E_p - E_{\pi^+})^2 - (p_p^x + p_{\pi^+}^x)^2 - (p_p^y + p_{\pi^+}^y)^2 - (p_p^z + p_{\pi^+}^z)^2$$

3.  $\rho^\circ$  cut. If the invariant mass squared calculated from the four momenta of the  $\pi^+$  and  $\pi^-$  is consistent with the  $\rho$ -meson mass,  $0.38 < m_{\pi^+\pi^-}^2 < 0.80 \text{ (GeV/c}^2\text{)}^2$ , we keep the event.
4.  $\Delta^{++}$  cut. We discard events that have invariant masses calculated from the  $\pi^+p$  pair consistent with the  $\Delta^{++}$  mass,  $1.26 < m_{\pi^+p}^2 < 1.80 \text{ (GeV/c}^2\text{)}^2$ .
5.  $\Delta^\circ$  cut. We discard events that have invariant masses calculated from the  $\pi^-p$  pair consistent with the  $\Delta^\circ$  mass,  $1.26 < m_{\pi^-p}^2 < 1.80 \text{ (GeV/c}^2\text{)}^2$ .

In Fig. 21 we plot the acceptance as a function of  $E_\gamma$  and  $t$  after all the above cuts have been imposed. We see the acceptance increases markedly as the energy of the incident photon increases. At  $E_\gamma = 1.4 \text{ GeV}$ , the acceptance  $\epsilon$  already is 0.11, and as the incident photon energy increases to 1.7 GeV,  $\epsilon$  more than doubles.

## A.4 Optimal Magnetic Field Setting

We studied the acceptance as a function of the magnetic field setting. We found that setting the field to maximum strength, with positive particles bending away from the beam, does not drastically alter the particle detection efficiency.

$\varepsilon = \varepsilon(E_\gamma, t)$  after all cuts. ( $B = +B_0$ )

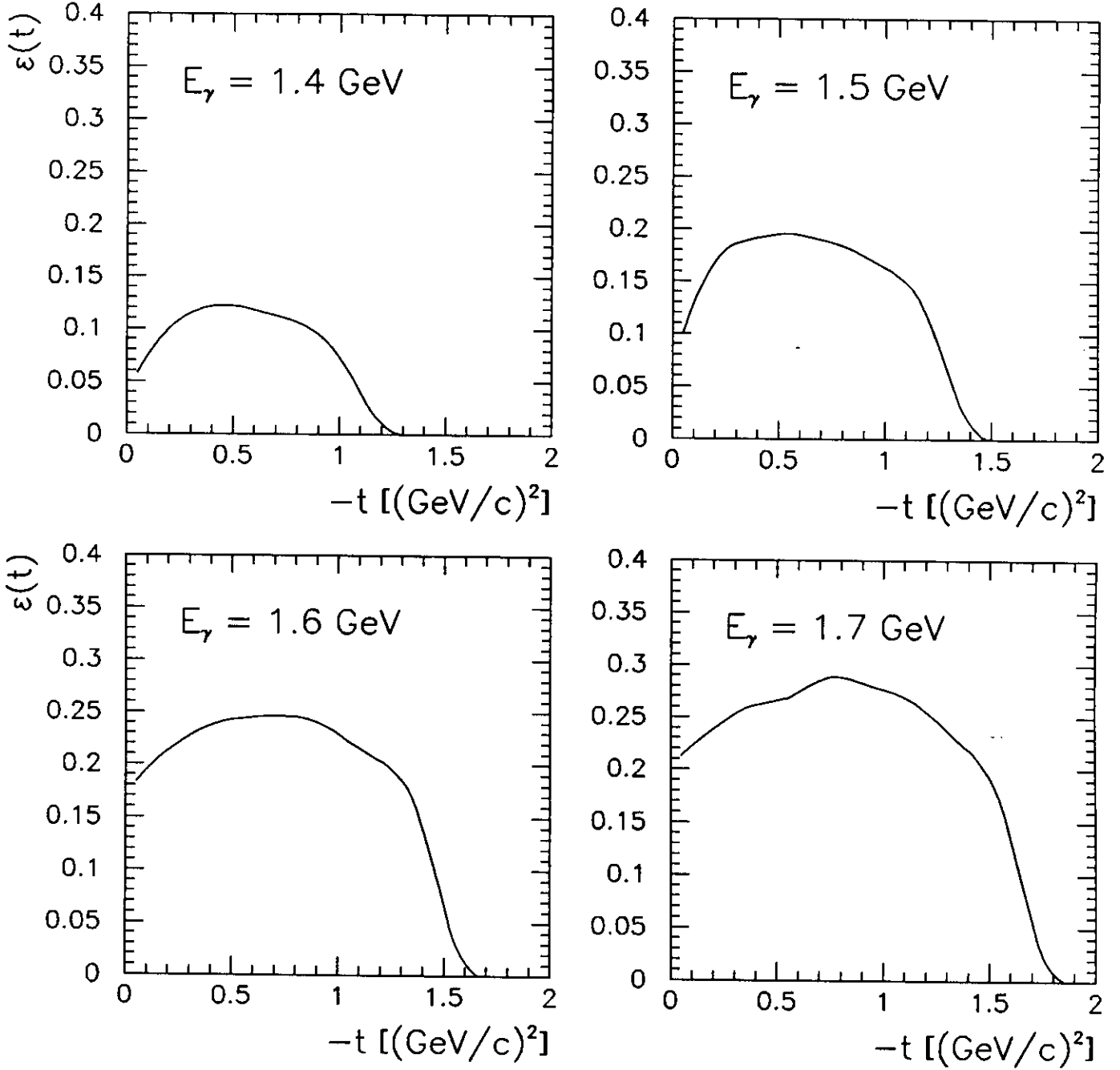


Figure 21: Acceptance plotted as a function of four-momentum transfer squared,  $-t$ , for four different incident photon energies.

We define the acceptance in the usual way:

$$\varepsilon = \frac{N_{\text{acc}}}{N_{\text{gen}}}$$

where  $N_{\text{gen}}$  is the total number of events generated and  $N_{\text{acc}}$  represents the numbers of events accepted after passing all cuts. Furthermore, the acceptance depends upon the incident tagged photon energy  $E_\gamma$  and upon both the strength and polarity of the toroidal field of the CLAS.

$$\varepsilon = \varepsilon(E_\gamma, \vec{B})$$

For these acceptance studies, 50 000 events were generated. We binned the acceptance in terms of

- $E_\gamma$ : 1.5, 1.7, 1.9, & 2.1 GeV
- B field: The magnetic field was set to  $-0.25$ ,  $+0.25$ ,  $+0.50$ ,  $+0.75$ , &  $+1.00$  times the nominal field strength.

In Table 6 we tabulate the number of events accepted under four separate cuts as a function of magnetic field setting and incident photon beam energy. Here, CutA means the first cut, i.e., the  $\pi^+$  and proton are mass identified in the event. CutB means events passing CutA with the addition constraints of (a) the missing mass being consistent with the mass of a pion and (b) the invariant mass of the  $\pi^+\pi^-$  pair falling within the fiducial mass range of the  $\rho$  meson. CutC describes events which satisfy the conditions for CutA and CutB, and the invariant mass of the  $\pi^+p$  pair is not consistent with the mass of the  $\Delta^{++}$ . Similarly, CutD is for accepted events which satisfy the selection criteria for CutA, CutB, and CutC, with the added condition that the invariant mass of the  $\pi^-p$  pair not be consistent with the mass of the  $\Delta^0$ . In Fig. 22a–c the acceptance as a function of incident photon energy under these cuts is plotted.

## A.5 Background

### A.5.1 $\gamma p \rightarrow \Delta\pi$

The primary source of  $2\pi$  background will come from  $\gamma + p \rightarrow \Delta(1232)\pi \rightarrow N\pi\pi$ . There are two reactions through the  $\Delta$  channel that lead to a  $\pi^+\pi^-p$  final state:

$$\gamma + p \rightarrow N^* \rightarrow \rho^0 + p$$

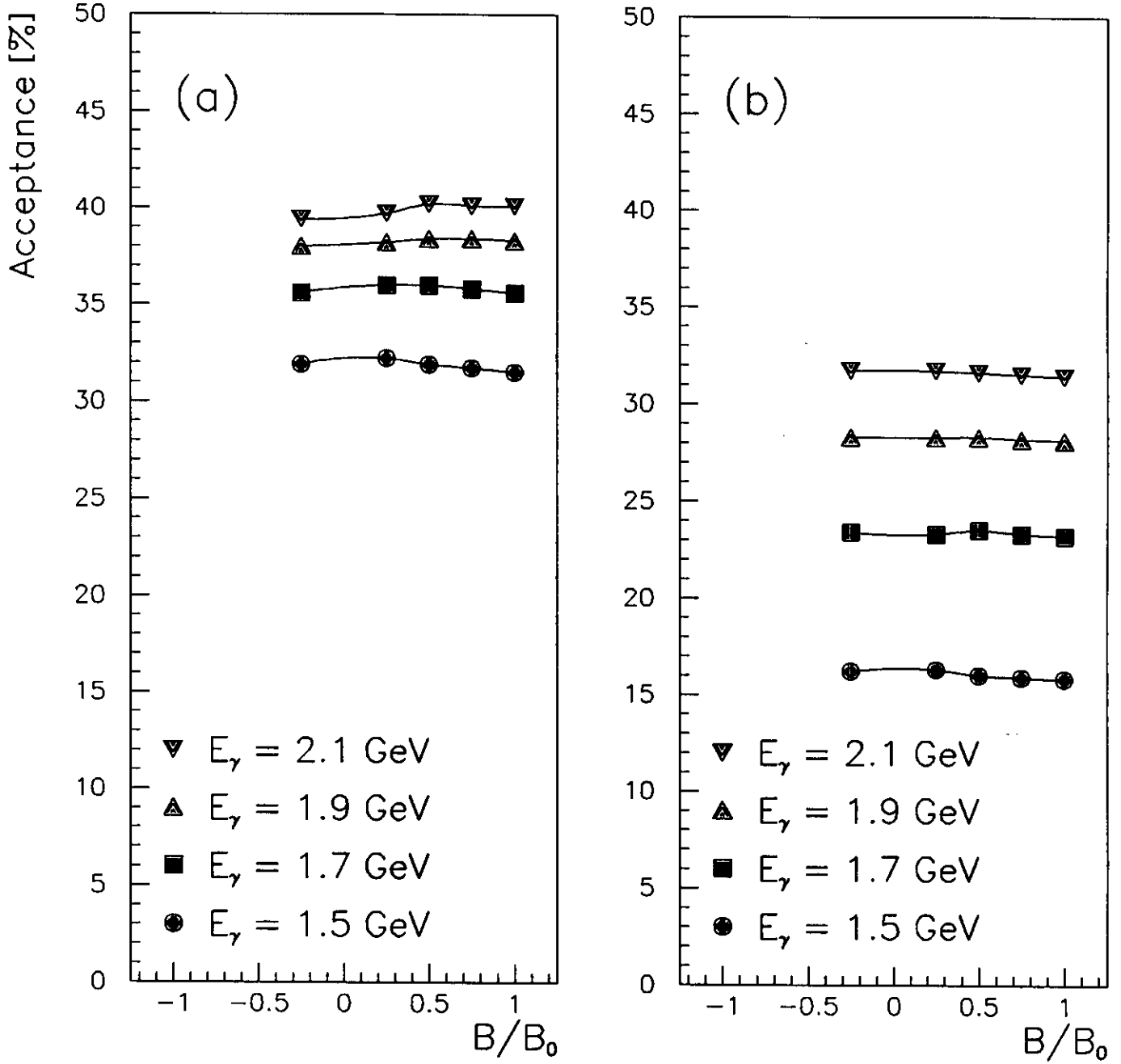


Figure 22: Acceptance of  $\gamma p \rightarrow \rho^0 p$ . The final-state particles,  $\pi^+$  and proton, are measured as a function of  $E_\gamma$  and  $B/B_0$  after imposing (a) cuts 1 through 4 and (b) cuts 1 through 5.

Table 6: Acceptance of  $\gamma + p \rightarrow \rho^0 + p$  events. See text for definitions of the cuts (50 000 events generated).

	$E_\gamma = 1.5 \text{ GeV}$				$E_\gamma = 1.7 \text{ GeV}$			
B/B <sub>0</sub>	CutA	CutB	CutC	CutD	CutA	CutB	CutC	CutD
-0.25	24236	23090	15971	8116	24852	23597	17850	11717
+0.25	24613	23516	16096	8161	25092	23999	17978	11760
+0.50	24484	23420	15925	7975	25038	24106	18005	11759
+0.75	24301	23175	15838	7950	24837	23879	17874	11643
+1.00	24074	22914	15736	7922	24640	23622	17792	11606

	$E_\gamma = 1.9 \text{ GeV}$				$E_\gamma = 2.1 \text{ GeV}$			
B/B <sub>0</sub>	CutA	CutB	CutC	CutD	CutA	CutB	CutC	CutD
-0.25	25177	23675	18994	14128	25266	23535	19700	15832
+0.25	25342	24040	19120	14167	25436	23892	19843	15871
+0.50	25305	24314	19192	14077	25429	24378	20114	15792
+0.75	25127	24139	19203	14123	25263	24211	20052	15730
+1.00	24926	23883	19148	14028	25069	23943	19994	15678

1.  $\gamma + p \rightarrow \Delta^{++} + \pi^-$
2.  $\gamma + p \rightarrow \Delta^0 + \pi^+$

The ratio of these cross sections can be written

$$R = \frac{\sigma(\gamma p \rightarrow \pi^- \Delta^{++})}{\sigma(\gamma p \rightarrow \pi^+ \Delta^0)} = \frac{|T(\gamma p \rightarrow \pi^- \Delta^{++})|^2}{|T(\gamma p \rightarrow \pi^+ \Delta^0)|^2}$$

and we note that based on isospin arguments [38],  $R = \frac{3}{4}$  for the intermediate resonance  $\Delta(I = \frac{3}{2})$ , and  $R = 3$  for the intermediate resonance  $N^*(I = \frac{1}{2})$ . The  $\Delta^0$  background will therefore need to be taken into account.

We employed the program GEN\_EVENT [39] to generate the  $\Delta^{++}$  reactions. The mass of the  $\Delta^{++}$  is Breit-Wigner distributed, and once the isobar mass is fixed, the  $\Delta^{++}$  and  $\pi^-$  are distributed uniformly in phase space via the Cernlib program GENBOD. The decay products of the  $\Delta^{++}$  are then distributed in the  $\Delta^{++}$  rest frame by employing the formula

$$\frac{d\sigma}{d\Omega} = A + B \cos \theta + C \cos^2 \theta$$

where the coefficients  $A$ ,  $B$ , and  $C$  are energy dependent and were taken from Ref. [40]. The algorithm for generating the events arising from the photoproduced  $\Delta^0$  channel is similar to the  $\Delta^{++}$  case.

In Table 7 we tabulate the number of  $\Delta$  background events that survive the  $\pi^-$  and  $\rho^0$  cuts (see subsection A.3). Imposing the  $\Delta^{++}/\Delta^0$  cut eliminates 96.0% of the background in the energy range of  $1.3 < E_\gamma < 2.1$  GeV (see Fig. 23a). Since the cross section for the reaction  $\gamma p \rightarrow \Delta^{++} \pi^-$  is approximately  $5 \mu\text{b}$  at  $|t| = 0.4 \text{ GeV}^2$  [22] in the energy range of  $1.4 < E_\gamma < 1.8$  GeV, as compared to  $10 \mu\text{b}$  at this value of  $|t|$  for photoproduced  $\rho^0$  mesons, the two-pion background will pose only minor problems for this experiment.

### A.5.2 $\gamma p \rightarrow \omega p$

The primary source of the  $3\pi$  background will come from photoproduced  $\omega$  mesons. In Table 8 we tabulate the number of events that survive our various cuts (see subsection A.4 for the definitions of the cuts). In Fig. 23b we plot the background acceptance as a function of cuts imposed and incident photon energy. We note that

$$\frac{\sigma(\gamma p \rightarrow \omega p)}{\sigma(\gamma p \rightarrow \rho^0 p)} \simeq \frac{1}{3}$$



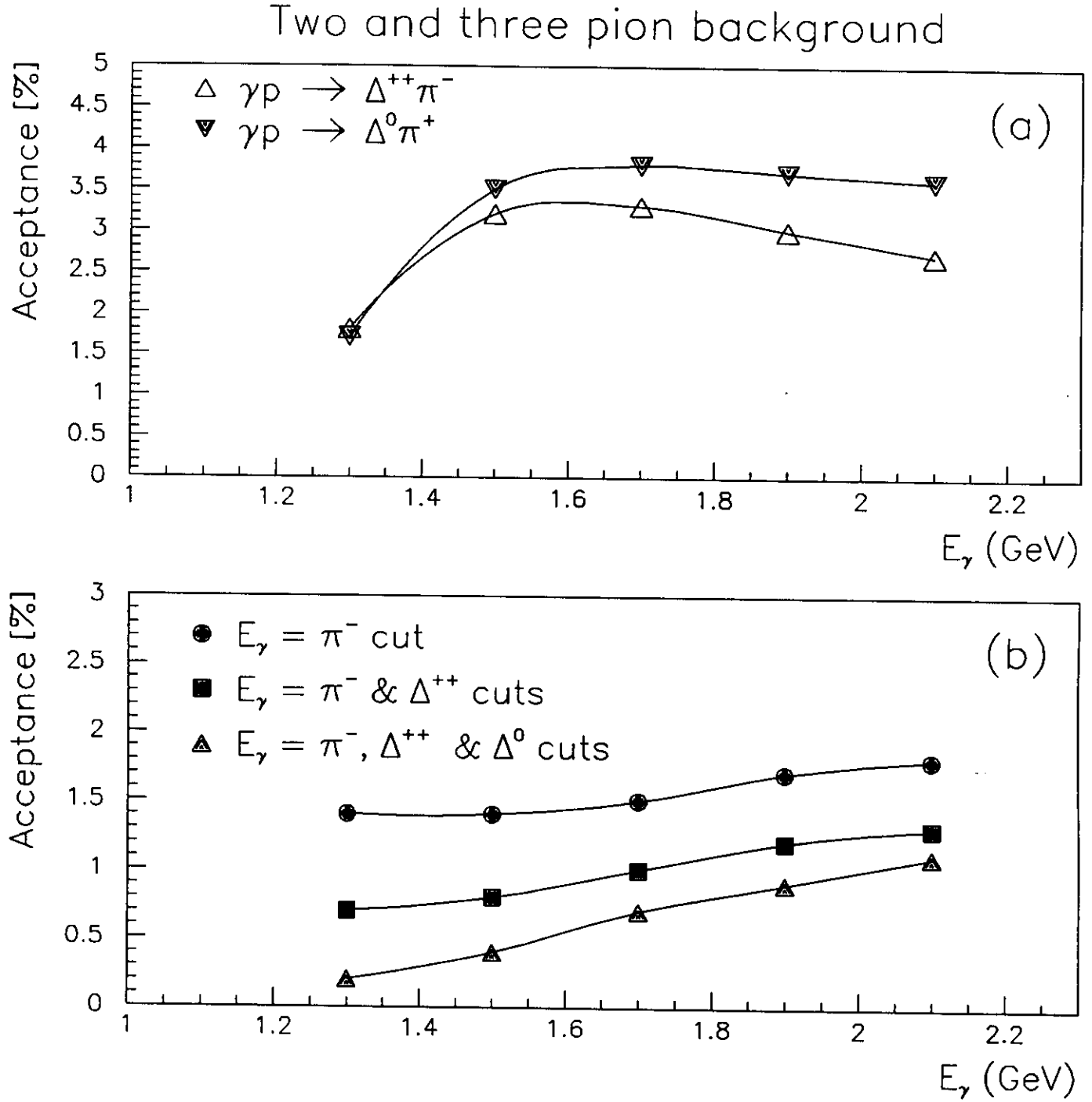


Figure 23: Background events that survive the acceptance cuts: (a) two-pion background arising from  $\gamma p \rightarrow \Delta \pi$  and (b) three-pion background arising from  $\gamma p \rightarrow \omega p$ .

Table 7: Acceptance of  $\gamma + p \rightarrow \Delta\pi$  events. See text for definitions of the cuts (50 000 events generated).

$E_\gamma$ [GeV]	$\gamma p \rightarrow \Delta^{++}\pi^-$		$\gamma p \rightarrow \Delta^0\pi^+$	
	$\pi^-$ cut	$\Delta^{++}$ cut	$\pi^-$ cut	$\Delta^0$ cut
1.3	11171	880	12004	856
1.5	11279	1707	12306	1732
1.7	9887	1653	11243	1895
1.9	8725	1508	10238	1836
2.1	7835	1354	9334	1775

at  $E_\gamma = 2.8$  GeV [12], [41]; thus, imposing all cuts, we see that the three-pion background will present absolutely no problems.

## A.6 Retrieval of the Density Matrix Elements

Because the acceptance is not a strong function of the magnetic field strength for positive polarities, we chose  $B = +B_0$  to minimize the uncertainty in the three momentum and maximize the detection of positively charged particles.

Before imposing the selection criteria on the event, we rotate and boost the pions to the helicity frame. We then calculate the probability density for a given  $\Delta \cos \theta_H \Delta \phi_H$  bin

$$W^{ij}(\cos \theta, \phi) = \frac{N_{\text{gen}}^{ij}}{N_{\text{gen}}^{\text{tot}}} \times \frac{1}{\Delta \cos \theta_H \Delta \phi_H}$$

We next impose our cuts on particle identification,  $\pi^-$ ,  $\rho^0$ ,  $\Delta^{++}$ , and  $\Delta^0$  mass, and count the number of events per each bin in  $\Delta \cos \theta_H \Delta \phi_H$ . Our efficiency can now be written:

$$\varepsilon = \frac{N_{\text{acc}}^{ij}}{N_{\text{gen}}^{ij}}$$

and we have (for  $\varepsilon \neq 0$ )

$$W^{ij}(\cos \theta, \phi) = \frac{N_{\text{acc}}^{ij}}{\varepsilon N_{\text{gen}}^{\text{tot}}} \times \frac{1}{\Delta \cos \theta_H \Delta \phi_H}$$

Table 8: Acceptance of  $\gamma + p \rightarrow \omega p$  events. See text for definitions of the cuts (50 000 events generated).

$E_\gamma$ [GeV]	CutA	CutB	CutC	CutD
1.3	20277	712	324	77
1.5	21258	698	400	208
1.7	21844	742	490	360
1.9	22019	831	576	451
2.1	21984	888	633	532

We note that

$$\varepsilon = \varepsilon(\sqrt{s}, t, \cos \theta_H, \phi_H)$$

Figure 24 shows a 3-dimensional depiction of  $W(\cos \theta, \phi)$  before cuts are imposed, for  $\sqrt{s} = 1.90$  GeV and  $0.8 < |t| < 0.9$  (GeV/c)<sup>2</sup>. Figure 25 shows the effects of imposing the various cuts on the angular distribution of the events in the helicity frame. As a matter of comparison, the events surviving the  $\Delta$  cuts for the reactions  $\gamma p \rightarrow \Delta^{++}\pi^-$  and  $\gamma p \rightarrow \Delta^0\pi^+$  are plotted in Fig. 26.

We can now solve for the various  $\rho_{\alpha\beta}^n$ s. First we observe that for  $\Phi = 0$ , the angular distribution can be written in the following form (cf. eq. 1)

$$\frac{4\pi}{3} W^{ij} = C^i + f_{11} \sin^2 \theta^i + f_{00} \cos^2 \theta^i + f_{10} \sin 2\theta^i \cos \phi^j + f_{1-1} \sin^2 \theta^i \cos 2\phi^j$$

Here, all angles are measured in the helicity frame, and the superscripts  $i$  ( $j$ ) refer to the  $i$ th ( $j$ th) bin in  $\theta_H$  ( $\phi_H$ ). For linearly polarized photons, the angular distribution can be decomposed into three terms,  $W(\cos \theta, \phi, \Phi) = W^0 - P_\gamma \cos 2\Phi W^1 - P_\gamma \sin 2\Phi W^2$ . Because the structure of  $W^0$  and  $W^1$  share  $\cos^2 \theta$ ,  $\sin 2\theta \cos \phi$ , and  $\sin^2 \theta \cos 2\phi$  terms, the density matrix elements  $\rho_{00}^1$ ,  $\text{Re}\rho_{10}^1$ , and  $\rho_{1-1}^1$  cannot be uniquely determined unless we already know  $\rho_{00}^0$ ,  $\text{Re}\rho_{10}^0$  and  $\rho_{1-1}^0$ . Therefore, we first determine the density matrix elements for the unpolarized case, and then use these values to constrain the density matrix elements that

$0.8 < -t < 0.9 \text{ (GeV/c)}^2$ ,  $\sqrt{s} = 1.90 \text{ GeV}$ ,  $\phi = 0^\circ$  and  $P_\gamma = 60\%$

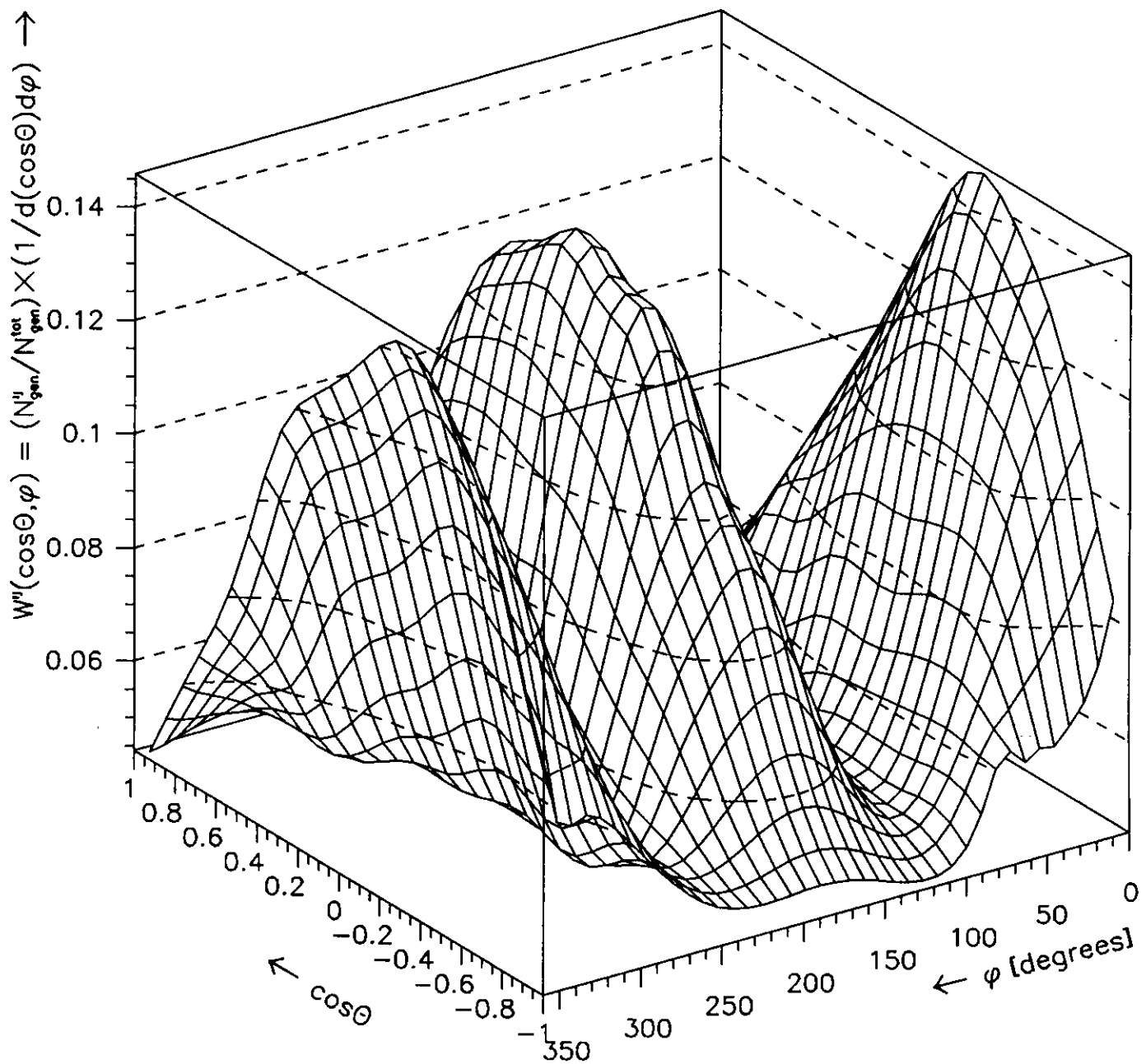


Figure 24: Surface plot of  $W(\cos\theta, \phi)$  before cuts are imposed.

$W(\cos\theta, \phi)$  Cuts in the Helicity Frame for  $\gamma p \rightarrow \rho^0 p$

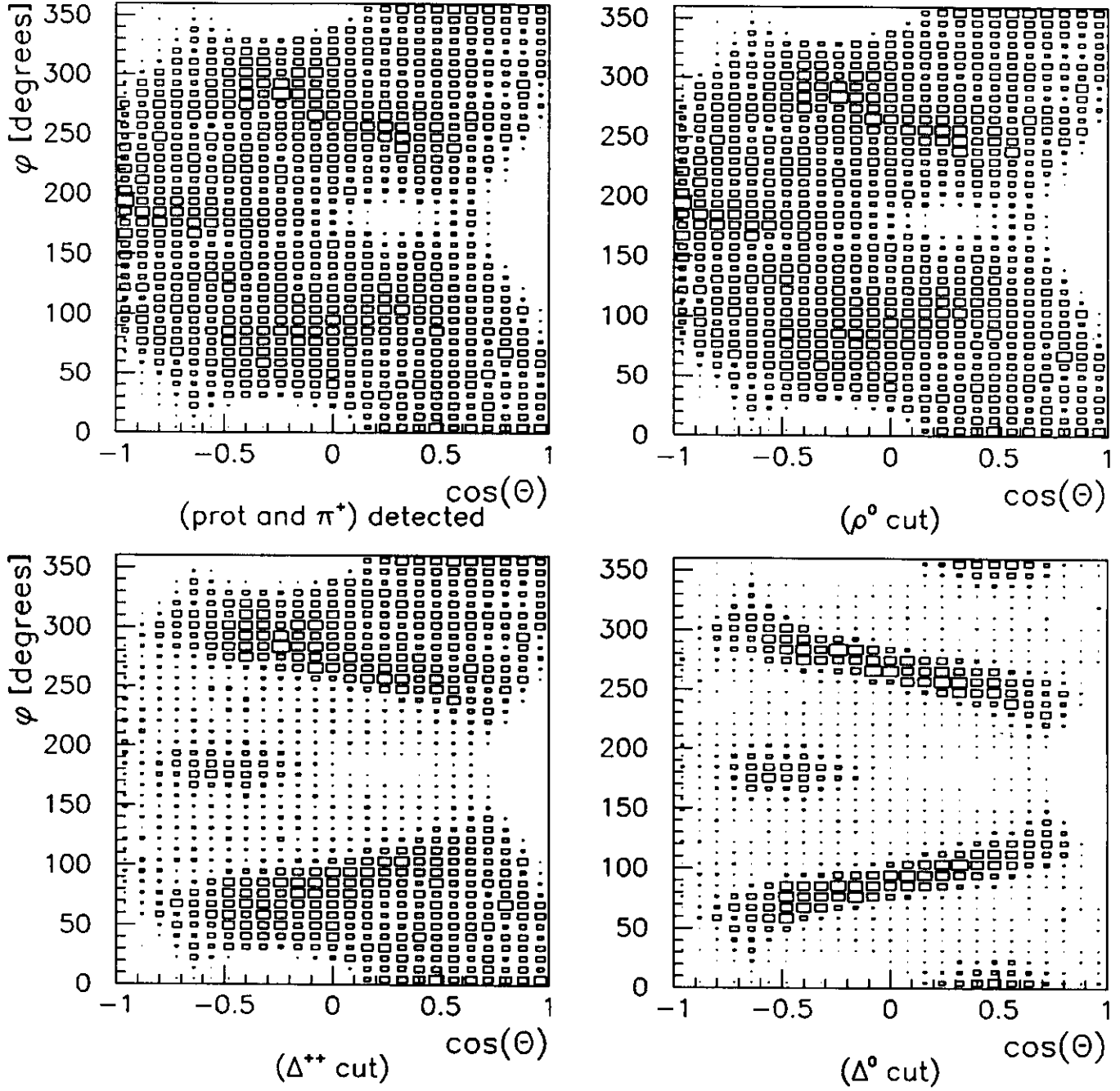


Figure 25: Effect of cuts on the helicity-frame angular distribution  $W(\cos\theta, \phi)$ .

$W(\cos\theta, \phi)$  Cuts in the Helicity Frame for  $\gamma p \rightarrow \Delta\pi$

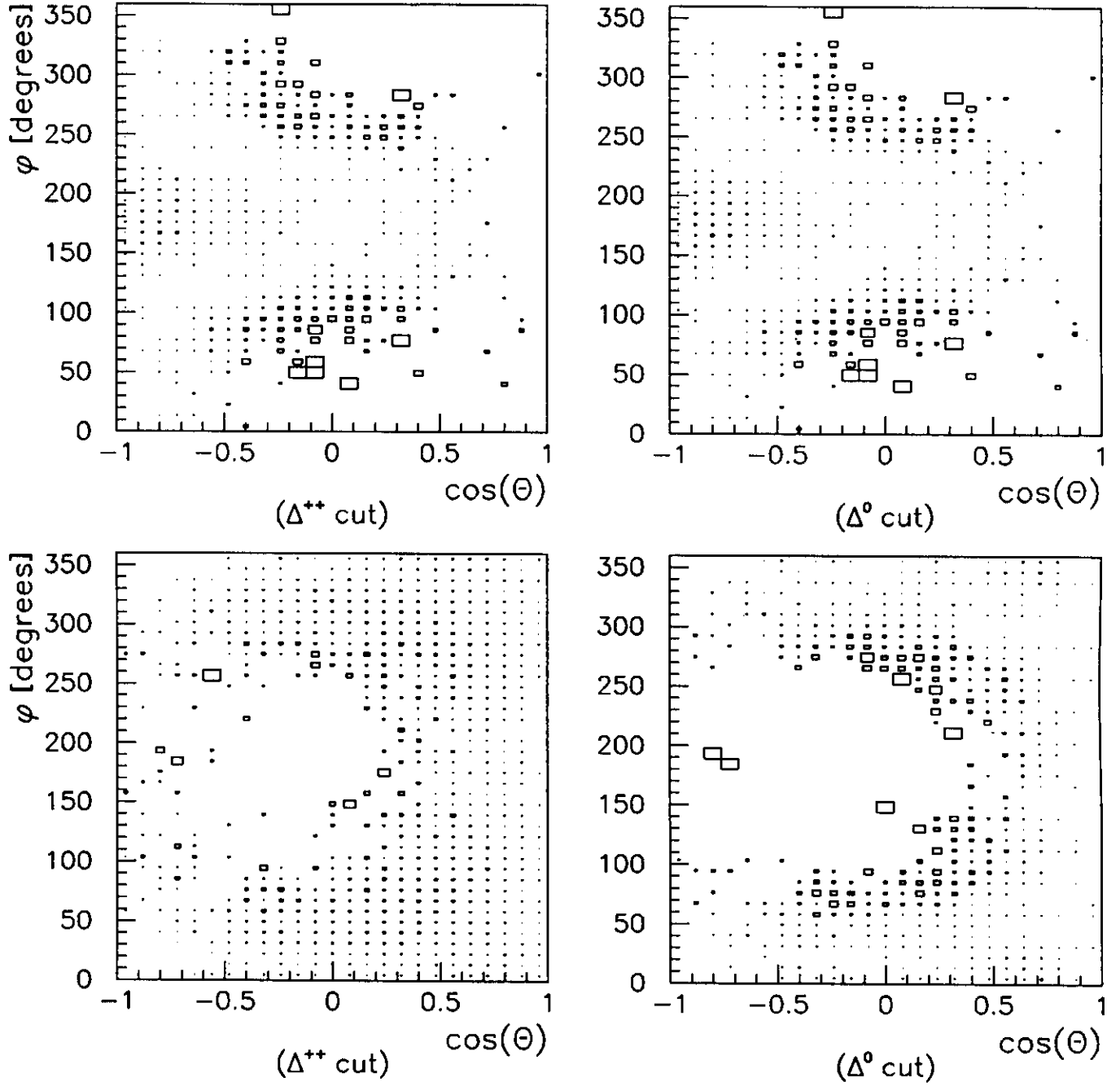


Figure 26: Effect of  $\Delta$  cuts on the helicity-frame angular distribution  $W(\cos\theta, \phi)$  for (above)  $\gamma p \rightarrow \Delta^{++}\pi^-$  and (below)  $\gamma p \rightarrow \Delta^0\pi^+$  ( $E_\gamma = 1.7$  GeV).

arise from linearly polarized photons.

This equation is of the form  $\mathbf{A} \cdot \mathbf{f} = \mathbf{b}$  where  $\mathbf{A}$  is a matrix (not necessarily square), and  $\mathbf{f}$  and  $\mathbf{b}$  are vectors. In order to solve for  $\mathbf{f}$ , we must invert the matrix  $\mathbf{A}$ . In Fig. 27, we plot the  $\Delta \cos \theta_H \Delta \phi_H$  bins containing at least 40 events, and having at least a 10% acceptance after selection criteria 1 through 5 are imposed for the unpolarized photon case. As an example, we generated 100 000 events in the range  $0.8 \leq -t < 0.9$  (GeV/c)<sup>2</sup> with  $\sqrt{s} = 1.90$  GeV ( $\Delta \cos \theta_H = 2/25$  and  $\Delta \phi_H = 2\pi/40$ , or 1000 bins in all). With these cuts, we still have over 100 equations for the three unknown density matrix elements,  $\rho_{00}^0$ ,  $\text{Re}\rho_{10}^0$ , and  $\rho_{10}^0$ . In order to solve this overdetermined set of linear equations and avoid singularities, we employed the technique of Singular Value Decomposition (SVD) [42] to invert  $\mathbf{A}$ . We found the solutions to be robust under alteration of the cuts; the values of the density matrix elements did not vary by more than a few percent. In Figs. 13a–c, we superimpose the retrieved density matrix elements onto the input density matrix curve arising from an unpolarized photon of energy 1.557 GeV ( $\sqrt{s} = 1.95$  GeV), plotted as a function of  $t$ . These retrieved spin density matrix elements are in excellent agreement with the input values.

For our studies of extracting the density matrix elements arising from a linearly polarized photon, we fixed the following parameters:

$$\begin{aligned}\sqrt{s} &= 1.90 \text{ GeV} \text{ (} E_\gamma = 1.455 \text{ GeV)} \\ \text{Polarization} &= 0.60 \\ \text{Polarization vector parallel to reaction plane} &(\Phi = 0^\circ)\end{aligned}$$

We have retrieved the density matrix elements for a few values of  $t$  (see Figs. 28a–d).

## A.7 Identification of the Charged Rho Channel

The identification of the  $\rho^+$  channel is much more difficult than the  $\rho^0$  one because there are three neutral particles and only one charged particle in the final state. Below we enumerate the selection criteria for the charged rho reaction:

1. Three neutrals and one positively charged particle in the final state.
2. Two photons measured in the electromagnetic shower counter.

$0.8 < -t < 0.9 \text{ (GeV/c)}^2$ ,  $\sqrt{s} = 1.90 \text{ GeV}$ ,  $\phi = 0^\circ$  and  $P_\gamma = 60\%$

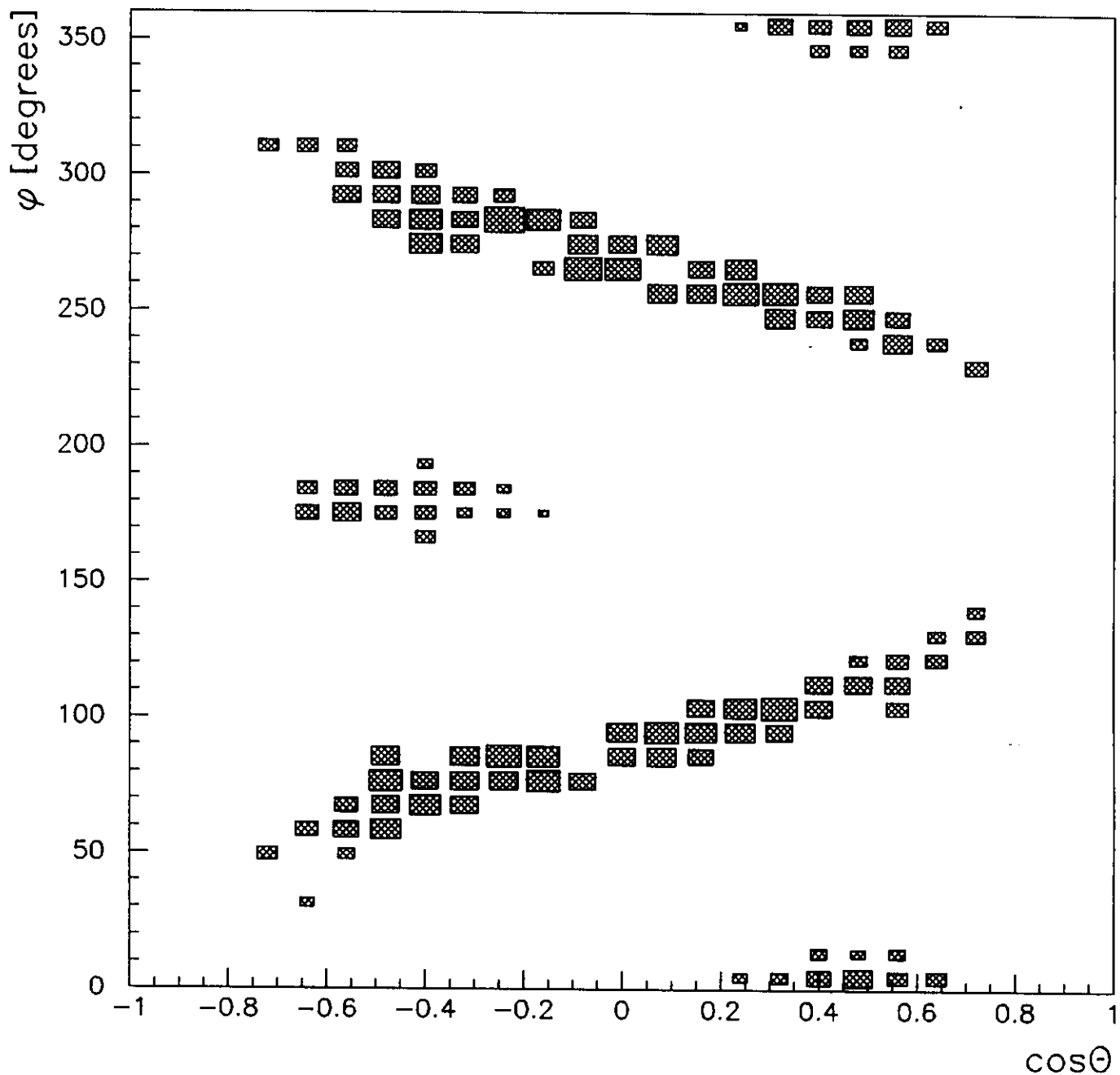


Figure 27: Accepted  $\pi^+$  events in the helicity frame after cuts 1 through 5 are applied. Each bin is required to contain at least 40 events and the bin acceptance is required to exceed 10%.



(60% Polarization  $\phi = 0$ )  $\sqrt{s} = 1.90$  GeV

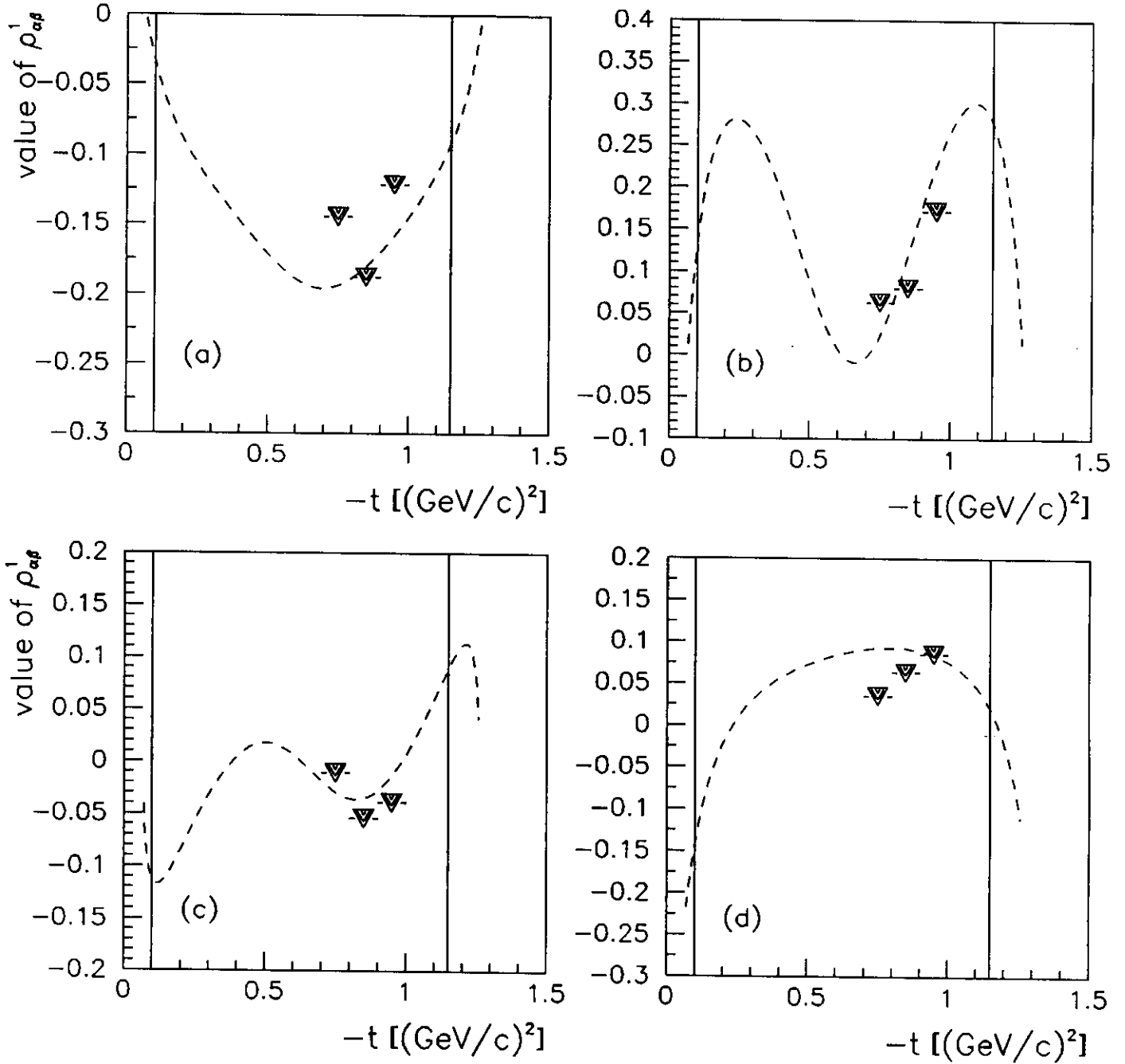


Figure 28: Retrieved density matrix elements after processing events through FastMC superimposed on input curve: (a)  $\rho_{11}^1$ ; (b)  $\rho_{00}^1$ ; (c)  $\text{Re}\rho_{10}^1$ ; and (d)  $\rho_{1-1}^1$ . The vertical lines denote the region of acceptance. The analysis is preliminary. We expect much better agreement upon application of more sophisticated mathematical techniques.

Table 9: Acceptance of  $\gamma + p \rightarrow \rho^+ + n$  events. See the text for definitions of the cuts (50 000 events generated).

	$E_\gamma = 1.7 \text{ GeV}$			$E_\gamma = 1.9 \text{ GeV}$			$E_\gamma = 2.1 \text{ GeV}$		
B/B <sub>0</sub>	Cut1	Cut2	Cut3	Cut1	Cut2	Cut3	Cut1	Cut2	Cut3
-0.25	2054	1347	1108	1827	866	1221	1223	609	1061
+0.25	2115	1411	1166	1850	864	1228	1251	655	1079
+0.50	2050	1312	1132	1629	950	1203	1227	619	1055
+0.75	2060	1342	1111	1558	906	1133	1274	636	1097
+1.00	2044	1377	1111	1574	896	1149	1252	654	1090

3. One neutron in the electromagnetic shower counter.

4.  $\pi^+$  mass identified.

5. A  $\rho^+$  cut of  $0.38 < m_{\pi^+\pi^0}^2 < 0.80 \text{ (GeV/c}^2\text{)}^2$ .

In Table 9 we tabulate the number of events accepted under three separate cuts as a function of magnetic field setting and incident photon beam energy. Here, Cut1 means the above five cuts. Cut2 signifies events satisfying the conditions of Cut1 and both of the following:

- $-0.05 < m_x^2 < 0.09 \text{ (GeV/c}^2\text{)}^2$ , where  $m_x$  is the missing mass from the neutron and  $\pi^+$ .

$$m_x^2 = (E_\gamma + m_{\text{prot}} - E_n - E_{\pi^+})^2 - (p_n^x + p_{\pi^+}^x)^2 - (p_n^y + p_{\pi^+}^y)^2 - (p_\gamma - p_n^z - p_{\pi^+}^z)^2$$

- $-0.05 < m_{\gamma\gamma}^2 < 0.09 \text{ (GeV/c}^2\text{)}^2$

The purpose of the mass cuts on both  $m_x^2$  and  $m_{\gamma\gamma}^2$  is to minimize  $2\pi^0$  background. In Fig. 29 the acceptance as a function of incident photon energy and magnetic field setting under Cut2 is plotted. Cut3 means events passing Cut1 and having four momentum transfer,  $|t| > 0.5 \text{ (GeV/c}^2\text{)}^2$ .

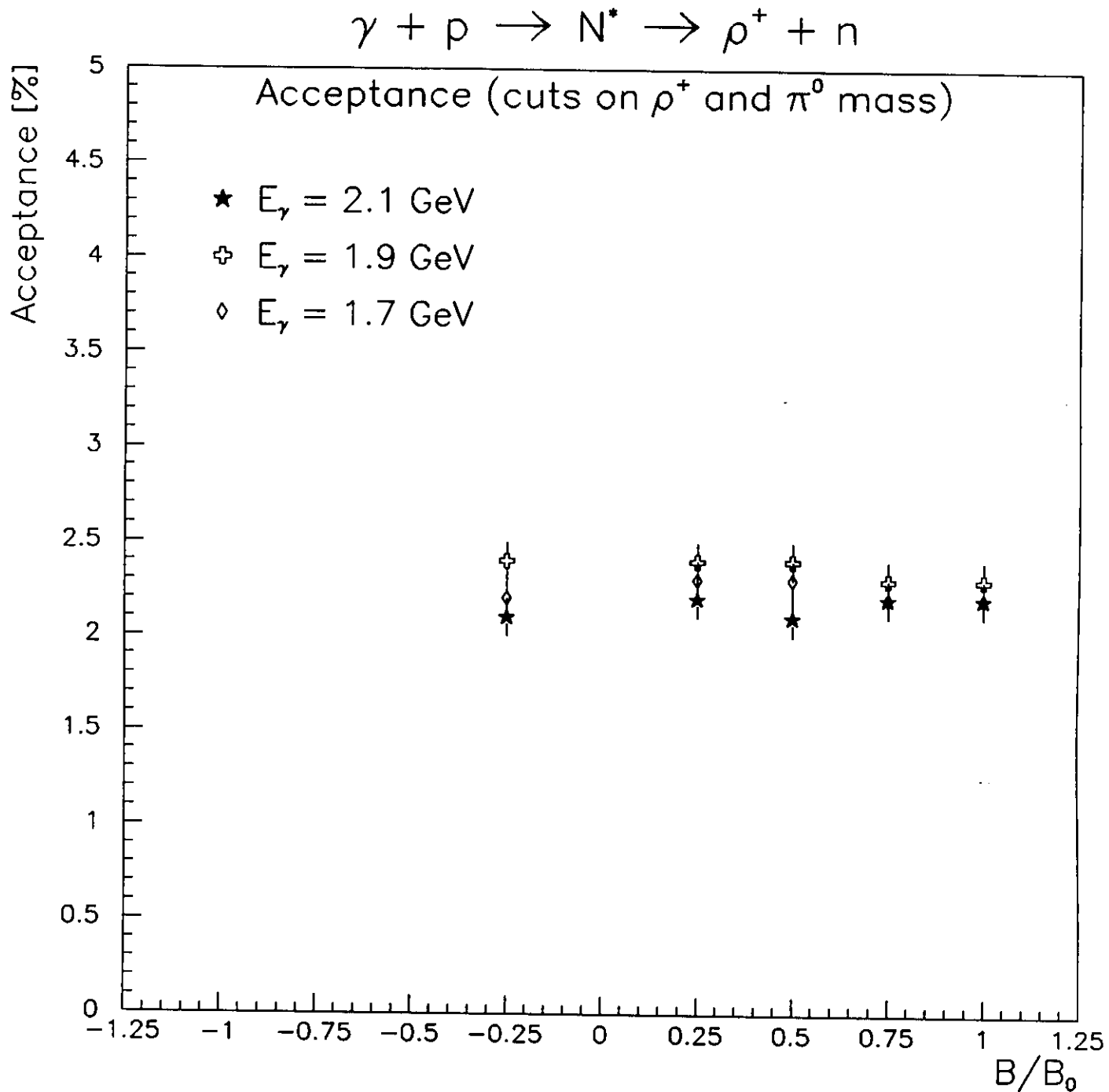


Figure 29: Acceptance of  $\gamma p \rightarrow \rho^+ n$ . All three neutral particles and one final-state charged particle are measured as functions of  $E_\gamma$  and  $B/B_0$ . Cut2 applies (see text).

We have not yet studied the angular distributions of the  $\pi^+$  in the helicity frame resulting from  $\rho^+$  decay. The analysis of extracting the density matrix elements of the decay products of  $\rho^+$  mesons will be identical to the  $\rho^0$  case. However, because of the expected reduced cross section of photoproduced  $\rho^+$  mesons (approximately one third that of the  $\rho^0$  mesons), and the acceptance being decreased by a factor of ten, it will be more difficult to extract the density matrix elements for the  $\rho^+$  than for the  $\rho^0$ . However, since no data exist for  $\bar{\gamma}p \rightarrow n\rho^+$ , even coarse binning will yield important results, and we still will be able to determine precise values for the asymmetry  $\Sigma$ .

## A.8 Status of the Acceptance Analysis

Simply using the SVD technique to invert the matrix of the overdetermined system of equations gives us the  $\rho_{\alpha\beta}^0$  with an analysis uncertainty of only a few percent. However, this technique is not ideal for the linear polarized case, since uncertainties as large as 30% come into play. We are presently studying other mathematical means of extracting the density matrix elements for the linear polarized case. In particular, we are investigating the techniques of maximum entropy and neural networks. The former technique has had considerable success in image processing, and the latter has been successfully employed in pattern recognition and track reconstruction. We fully expect to reduce the discrepancy between the retrieved and input density matrix elements for the linearly polarized case to the 10% level or better upon application of these (or other) more refined mathematical methods.

## B Photon Polarization by Coherent Bremsstrahlung

The spectrum of a photon beam produced coherently from a crystal radiator has several distinguishing characteristics compared with incoherent bremsstrahlung. The spectrum exhibits discrete peaks of high intensity, with strong linear polarization within the peaks. The multiplicity of peaks results from coherent bremsstrahlung from more than one reciprocal lattice vector in the crystal. In order to obtain the best linear polarization, it is necessary to choose a crystal with a well isolated lattice vector, and orient the crystal so that one peak is maximized and contributions from other lattice sites are minimized. Another characteristic is that the angular distribution of the coherent photons is correlated with photon energy such that tight collimation can be used to reduce the incoherent background without significantly affecting the peak of the coherent spectrum.

Data from SLAC, shown in Fig. 30 [31], show an intensity spectrum produced by a 19.7 GeV electron beam incident on a 47  $\mu\text{m}$  thick diamond crystal. The large coherent peak at 10 GeV corresponds to the (0,2,2) lattice vector; several smaller peaks can be seen at higher energies, corresponding to other lattice vectors [primarily (0,4,4) and (0,8,8)]. This satisfies our requirements for a well isolated coherent peak. We plan to use a thinner (10  $\mu\text{m}$ ) diamond crystal as the radiator oriented to maximize the contribution from the (0,2,2) lattice vector, because a thinner crystal will produce a spectrum less contaminated by coherent bremsstrahlung from the other crystalline directions.

The energy of the coherent peak is related to the longitudinal projection of the reciprocal lattice vector by

$$q_L = \frac{m^2 x (1 + \theta^2)}{2E_0(1 - x)},$$

where  $\theta$  is the divergence angle of the coherently produced photons,  $E_0$  is the electron energy,  $m$  is the electron mass, and  $x = k/E_0$  is the fractional photon energy. The maximum fractional energy that can be obtained for a given crystal orientation is related to the minimum longitudinal momentum by setting  $\theta = 0$ . In Fig. 14, we show the results of our Monte Carlo calculation [43] for coherent bremsstrahlung from the (0,2,2) lattice in a 10  $\mu\text{m}$  diamond crystal. The spectrum shows a cutoff of the coherent peak at 1.7 GeV corresponding to the maximum fractional energy for the assumed crystal orientation. The input parameters for our calculation are given in Table 10.

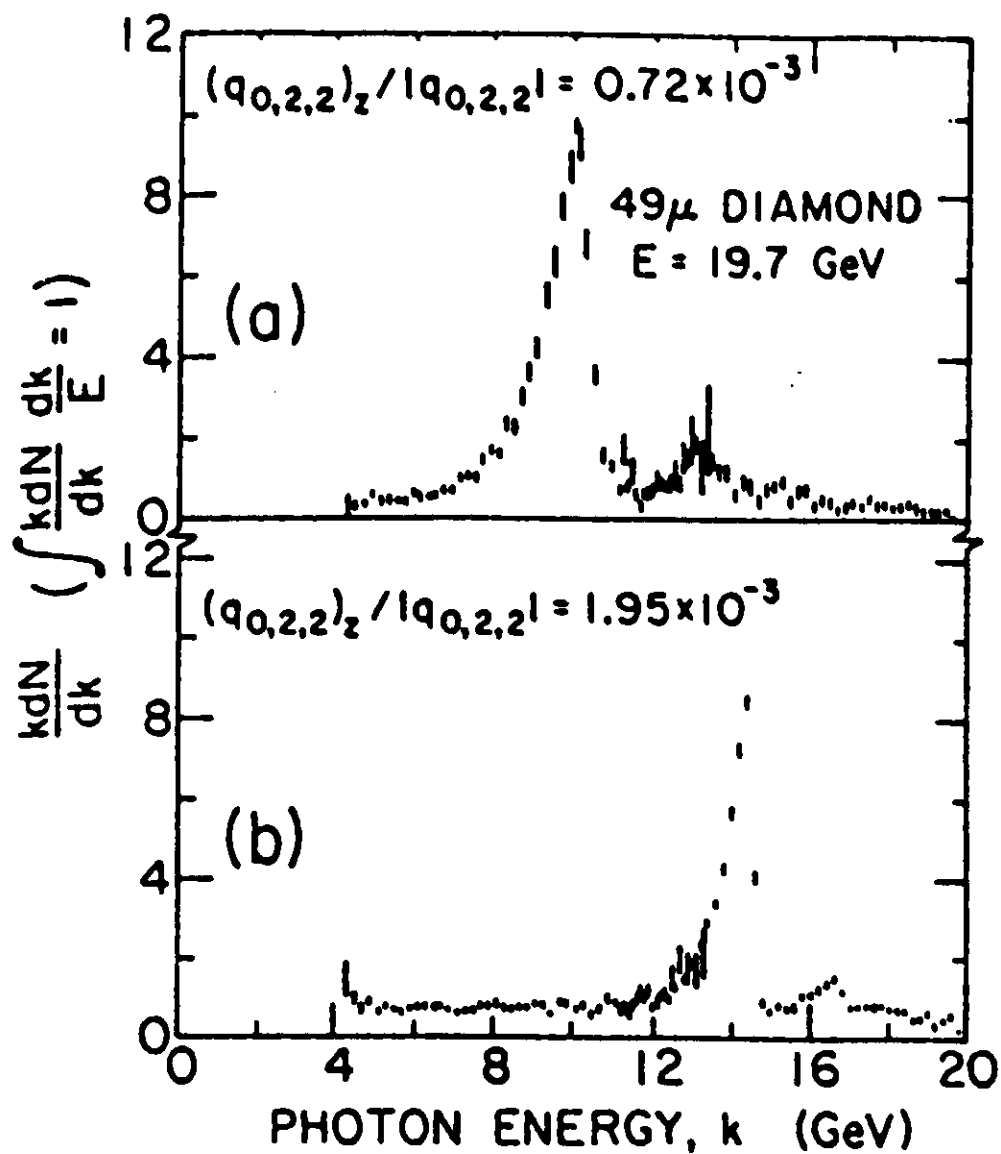


Figure 30: Coherent bremsstrahlung spectrum from SLAC with a 19.7 GeV electron beam and a  $47 \mu\text{m}$  diamond crystal radiator. The measured intensity distribution of the (a) 10 GeV setting and (b) 14 GeV setting.

Table 10: Input Parameters for Coherent Bremsstrahlung Monte-Carlo Calculation.

Electron Energy	6 GeV
Energy spread ( $dE/E$ )	$5 \times 10^{-5}$
Horizontal beam diameter	$5 \times 10^{-4}$ m
Horizontal beam emittance	$4 \times 10^{-9}$ m·rad
Vertical beam size	$5 \times 10^{-4}$ m
Vertical beam emittance	$4 \times 10^{-9}$ m·rad
Beam current	100 nA
Beamtime	1 second
Crystal thickness	10 $\mu$ m
$k/E_0^{\max}$	0.283
Angle of (0,2,2) lattice vector from vertical	873 $\mu$ rad
Azimuthal angle of (0,2,2)	90°

The energy (or  $x_{\max}$ ) at the peak of the coherent spectrum can be tuned by the choice of the crystal orientation. The lower the  $x_{\max}$  value chosen, the higher the degree of linear polarization within the coherent peak. The maximum fractional photon energy can be lowered either by orienting the crystal so that the peak appears at a lower photon energy (decreasing  $q_\ell$ ), or by increasing  $E_0$ . In Fig. 31, we show a comparison of polarization spectra obtained by 4 GeV and 6 GeV electron beams, with  $k_{\max}$  for both cases constrained to be 1.7 GeV. The enhancement in polarization going from a 4 GeV to a 6 GeV beam for  $E_\gamma = 1.7$  GeV is from 0.5 to 0.73.

The direction of linear polarization, specified by the  $\vec{\epsilon}$  orientation of the photon, can be changed by rotating the diamond crystal. This is important in a  $4\pi$  detector such as CLAS, in order to reduce systematic uncertainties. Earlier counter experiments using linearly polarized beams used the technique of changing the crystal orientation to the (0,2,-2) lattice vector [located 90° relative to the (0,2,2) lattice vector] in order to change the direction of the photon spin orientation and to extract the polarization asymmetry  $\Sigma$  [44]. The asymmetry depends upon the angle  $\psi = \phi_H - \Phi$ , where  $\phi_H$  is the azimuthal angle of the  $\pi^+$  in

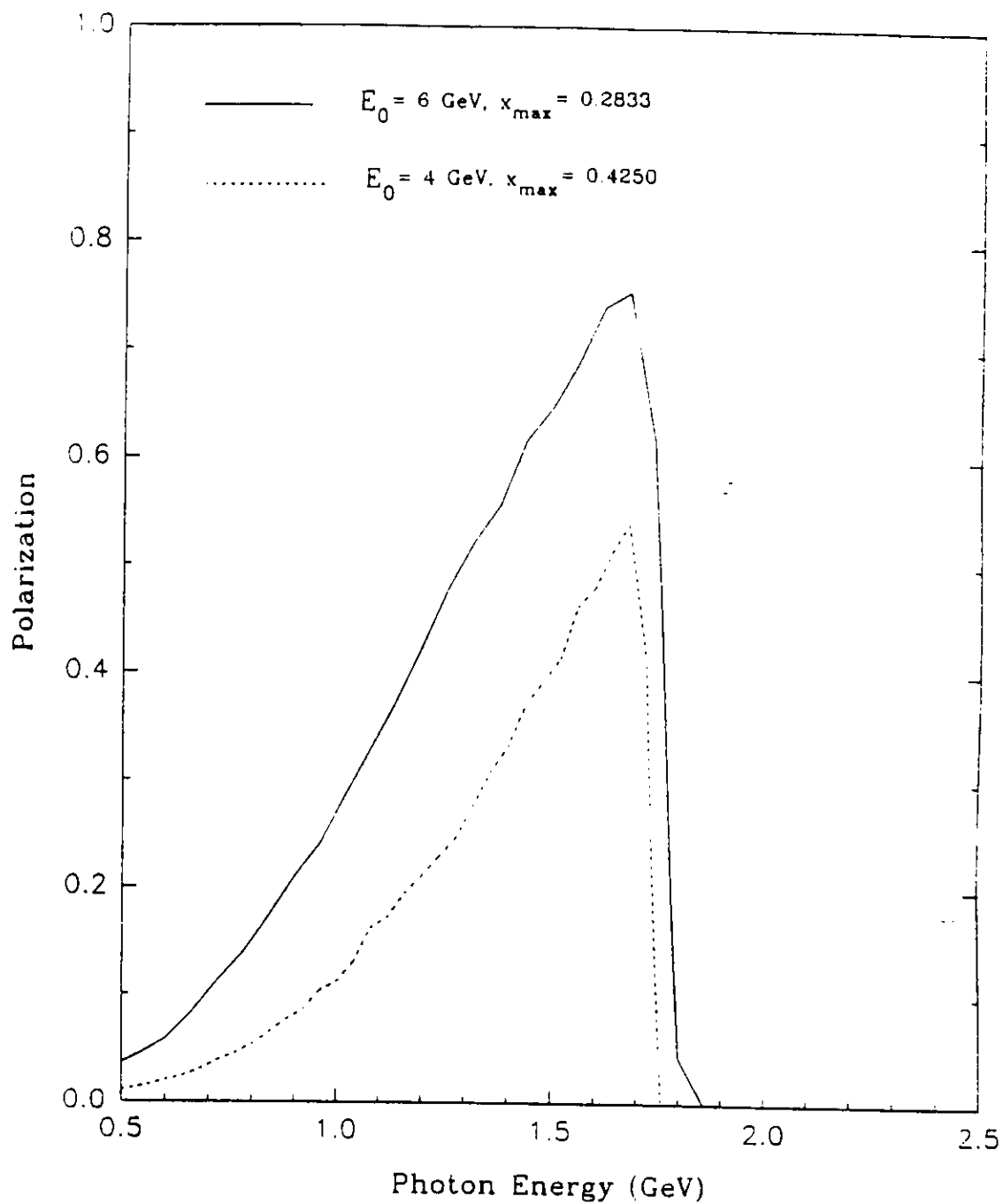


Figure 31: Comparison of polarization spectra from 4 and 6 GeV beams from our simulations. The diamond crystal has been oriented for both cases to give the maximum coherence at 1.7 GeV.



the helicity frame and  $\Phi$  is the azimuthal angle of the photon polarization vector. With CLAS, we are able to sample  $\psi = 0^\circ$  and  $\psi = 90^\circ$  simultaneously, as well as all other angles in between. However, we also plan to change the polarization direction during the running of the experiment in order to reduce any remaining systematic uncertainties from CLAS.

In its most basic design, a coherent bremsstrahlung facility is relatively simple to implement. A supply of thin diamond crystals needs to be obtained. Although the crystalline structure of the diamond may be degraded after prolonged exposure to the beam, the low beam currents expected in Hall B will ensure that the lifetime of a given crystal will extend well beyond the running time of any particular experiment. We calculate that for a 100 nA electron beam with a 0.5 mm ( $\sigma$ ) diameter spot size, the lifetime of a 10  $\mu$ m thick crystal should be 24 days. We will also need to procure a precision goniometer with three rotational degrees of freedom and with a  $x$ - $z$  translational capability. The goniometer will need an 11  $\mu$ rad step size; this precision will enable the energy of the coherent peak to be moved in 15 MeV steps. The goniometer and diamond crystals can both be purchased at a relatively modest cost. The Hall B beamline working group is aware of the (minimal) requirements of the coherent bremsstrahlung facility in terms of space near the radiator and the size of the beampipe needed to accommodate the goniometer.

Two technical challenges remain. First is the question of more restrictive collimation. As mentioned above, the coherent part of the photon beam is more forwardly focused than the incoherent part. With very tight collimation, on the order of one characteristic angle  $\theta_C$  (at 6 GeV,  $\theta_C = 90 \mu$ rad), corresponding to an aperture size of 1.4 mm, 8 meters from the radiator, a large part of the incoherent spectrum can be suppressed. The result is an increase in polarization under the coherent peak, since the incoherent background reduces the polarization. The collimator now planned to be installed in the beamline would collimate only to  $\theta = 620 \mu$ rad. The primary difficulty in using a small aperture collimator is devising a reliable method to align the collimator along the  $\theta = 0^\circ$  axis. This problem has been addressed satisfactorily at SLAC where a 2 mm diameter collimator has been aligned along the beam 90 meters from the radiator. In Fig. 32 are plotted two polarization spectra, one showing the polarization with tight (1 mm aperture) collimation and one with the anticipated standard Hall B collimator. The tight collimation results in a substantial increase in polarization, from 0.73 to 0.93, at the peak. This increased polarization will

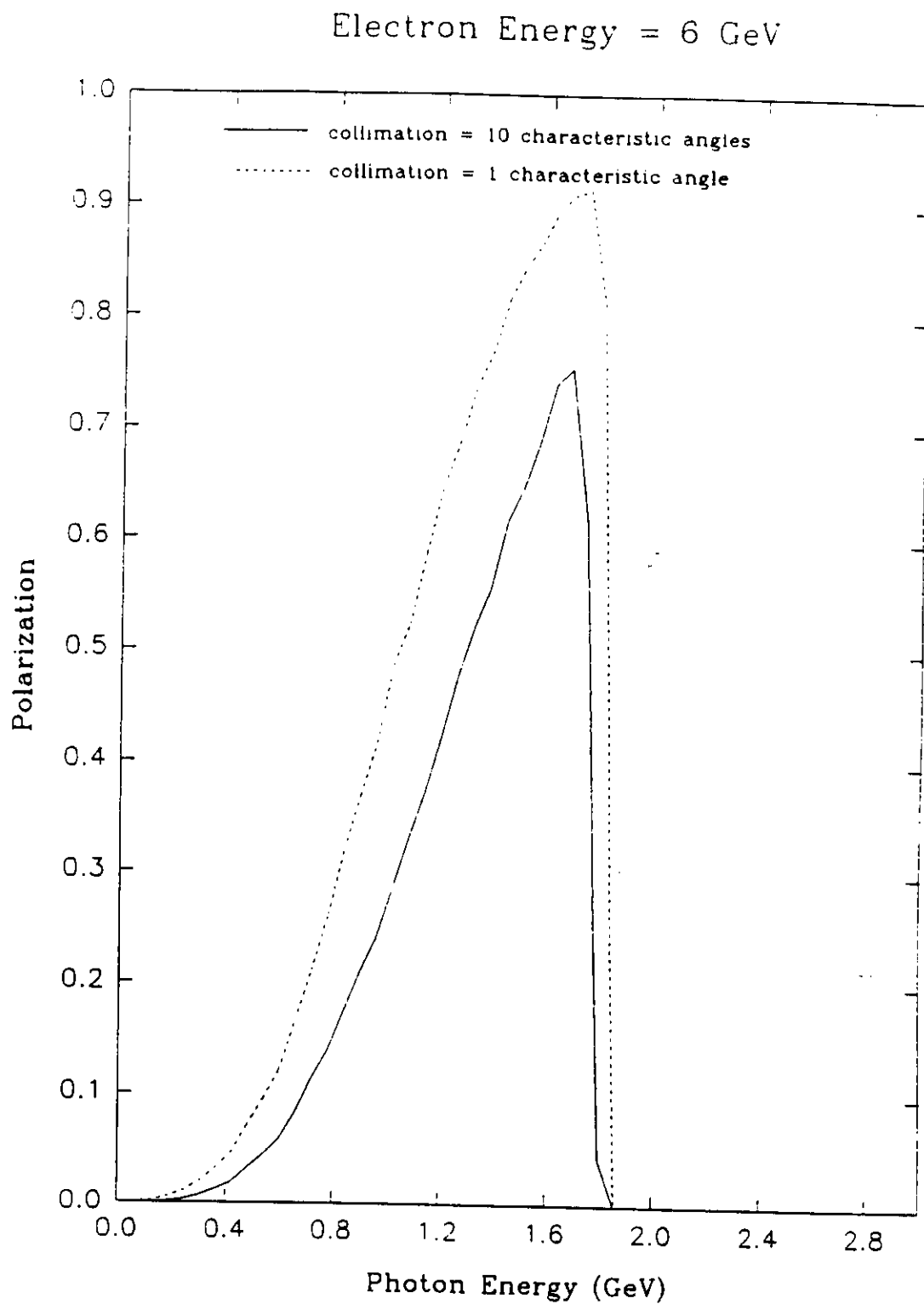


Figure 32: Comparison of polarization spectra at  $E_0 = 6$  GeV, showing the effect of tight collimation (1 characteristic angle) compared with that for the expected Hall B collimation.

allow us to decrease the bin size and thus heighten our sensitivity to small effects. For this reason, we will use a photon beam collimated to 1 characteristic angle. One option we are investigating is placing the crystal radiator 10 meters upstream from the normal radiator position, i.e. 18 meters distant from the collimator. The effect from the optics of the tagging magnet would be small and the size of the collimator hole could be increased to 3.2 mm.

The second technical challenge that must be met, common to all polarized-photon experiments, is the method of determining the polarization. We will discuss three methods. For our experiment, we will take advantage of the nature of diffractive  $\rho^0$  production by looking at very low- $t$  data where the large diffractive cross section has been determined to have a polarization asymmetry of  $\Sigma = 1$  for a polarized beam with  $P_\gamma = 1$ . For other polarizations,  $\Sigma$  is proportional to the reciprocal of the beam polarization. This method of determining the polarization has been used with success by Diambrini-Palazzi *et al.* [47]; they cite a 2% uncertainty in the beam polarization. We expect to attain a comparable uncertainty in the beam polarization. A second method is based upon the phenomenon of triplet production in the electron-positron creation process. In the photo-creation of an electron-positron pair in the electric field of an electron, the azimuthal distribution of the recoil electrons is correlated with the linear polarization of the incident photons [45]. The recoil electrons with large angles and energies of several MeV are easily measured. A polarimeter of this sort has been built by the Tokyo group [46] for use with a coherent bremsstrahlung photon beam and a photon tagger. Although they were limited in their statistics due to the 10.5% duty factor of the accelerator, their initial results were encouraging. A third less satisfactory method is to calculate the polarization spectrum from the well-known formulas for coherent bremsstrahlung and compare the calculation with the spectrum obtained in the tagger. This method has been used in the past (*e.g.*, Ref. [31]) but has the disadvantage of being model dependent and large systematic uncertainties will result. However, the data from the tagger will come free of cost and this method will serve as a check for other polarization determinations.

The physics goals of this experiment can be achieved by using a coherent bremsstrahlung source, and we have chosen to pursue this approach because we feel it has the greatest probability of succeeding. Our collaboration, in fact, will take a leading role in the design, construction and implementation of all aspects of the coherent bremsstrahlung facility.

However, recent developments in mirror and laser technology give reason for optimism that the Compton-backscattering source proposed in the update to LOI-93-12 [48] will be able to deliver  $10^5/\text{s/MeV}$   $\vec{\gamma}$ 's at energies up to 1.8 GeV. If successfully implemented, this source would provide a photon beam of high and precisely known polarization from threshold to 1.8 GeV, would have a tagging efficiency approaching 100%, would be essentially free of backgrounds and untagged photons, and would make possible asymmetry measurements of high precision across a useful range of kinematics. We will use the Compton source if it is available when this experiment is scheduled to run, for that part of the experiment for  $E_\gamma \leq 1.8$  GeV, if it produces improved results for the same amount of beamtime.

# References

- [1] D.B. Lichtenberg, Phys. Rev. 178, 2197 (1969);  
R.E. Cutkosky and R.E. Hendrick, Phys. Rev. D 16, 2902 (1977).
- [2] R. Koniuk and N. Isgur, Phys. Rev. D 21, 1868 (1980).
- [3] S. Capstick and N. Isgur, Phys. Rev. D 34, 2809 (1986).
- [4] S. Capstick and W. Roberts, Phys. Rev. D 47, 1994 (1993).
- [5] "A Search for Missing Baryons Formed in  $\gamma p \rightarrow p\pi^+\pi^-$  using the CLAS and CEBAF," CEBAF Proposal E-93-033, J. Napolitano spokesperson.
- [6] V.D. Burkert, "Electromagnetic Excitation of Nucleon Resonances," CEBAF-PR-94-005, the relevant list of approved  $N^*$  experiments are contained in Table 1 of this reference.
- [7] R. Arndt *et al.*, Phys. Rev. D 43, 2131 (1991).
- [8] Z.L. Li, Ph.D. thesis, Virginia Polytechnic Institute, (1992).
- [9] D.M. Manley and E.M. Saleski, Phys. Rev. D 45, 4002 (1992).
- [10] D.M. Manley,  $\pi N$  Newsletter No. 8, 141 (1993).
- [11] K. Schilling *et al.*, Nucl. Phys. B 15, 397 (1970).
- [12] J. Ballam *et al.*, Phys. Rev. Lett. 24, 960 (1970).
- [13] D. Schildknecht and B. Schrempp-Otto, Nuovo Cim. 5A, 103 (1971).
- [14] W. Roberts, *Report to the GRAAL Group on Photoproduction of Baryon Resonances Using Polarized Photons* (1994), unpublished.
- [15] S. Capstick and W. Roberts, Phys. Rev. D 49, 4570 (1994).
- [16] S. Capstick, Phys. Rev. D 46, 1965 (1992);  
S. Capstick, Phys. Rev. D 46, 2864 (1992).
- [17] S. Capstick and B.D. Keister, Phys. Rev. D 47, 860 (1993).
- [18] S. Capstick, B.D. Keister, and W. Roberts, work in progress.
- [19] R.L. Anderson *et al.*, Phys. Rev. D, 679 (1976).
- [20] R.L. Anderson *et al.*, Phys. Rev. D 1, 27 (1970).
- [21] R.W. Clift *et al.*, Phys. Lett. B 64, 213 (1976).
- [22] Aachen-Berlin-Bonn-Hamburg-Heidelberg-München Collaboration, Phys. Rev. 175, 1669 (1968).
- [23] R. Erbe *et al.*, Nuovo Cim. 48, 262 (1967).
- [24] H.G. Hilpert *et al.*, Nucl. Phys. B 21, 93 (1970).
- [25] L. Criegee *et al.*, Phys. Rev. Lett. 25, 1306 (1970).
- [26] P. Benz *et al.*, Nucl. Phys. B 79, 10 (1974).

- [27] M. Davier *et al.*, Phys. Rev. D 1, 790 (1970).
- [28] D.P. Barber *et al.*, Z. Phys. C 2, 1 (1979).
- [29] P.L. Cole, "An Event Generator for Helicity Frame Angular Distributions," CLAS-NOTE in progress.
- [30] B. Norum, *private communication* (1994).
- [31] W. Kaune *et al.*, Phys. Rev. D 11, 478 (1975).
- [32] G. Diambri-Palazzi, Rev. Mod. Phys. 40, 611 (1968).
- [33] D.I. Sober, *private communication* (1994).
- [34] P.L. Cole, "A Generalized FASTMC for the CLAS," CLAS-NOTE 93-006.
- [35] E.S. Smith, "FAST Monte Carlo for the CLAS Detector," CLAS-NOTE 90-003.
- [36] J. Napolitano, *private communication* (1994).
- [37] V.D. Burkert, *private communication* (1994).
- [38] D.M. Manley, *private communication* (1994).
- [39] L. Murphy, Ph.D. thesis, *Double Pion Photon Production on Single Nucleons from Threshold up to 780 MeV*, Rensselaer Polytechnic Institute (1993).
- [40] G. Fischer *et al.*, Nucl. Phys. B, 93 (1970).
- [41] J. Ballam *et al.*, Phys. Rev. Lett. 24, 1364 (1970).
- [42] W.H. Press, W.T. Vetterling, S.A. Teukolsky, and B.P. Flannery, "Numerical Recipes in FORTRAN," Cambridge University Press, 2/e (1992).
- [43] S.L. Rugari, "A Coherent Bremsstrahlung Facility to Produce Monochromatic Polarized Photons at CEBAF Hall B," CLAS-NOTE *to be submitted*.
- [44] G. Wolf, "Photoproduction of Vector Mesons" *Springer Tracts in Modern Physics*, 59, 77 (1971).
- [45] V.F. Boldyshev and Yu. P. Peresun'ko, Sov. J. Nucl. Phys. 14, 576 (1972).
- [46] Y. Iwata *et al.*, Nucl. Instrum. Methods A 336, 146 (1993).
- [47] G. Diambri-Palazzi *et al.*, Phys. Rev. Lett. 25, 478 (1970).
- [48] P. Welch, B. Norum, K. Wang, and C. Keppel, LOI 93-12 Status Update, Dec. 1994.
- [49] K.-H. Krause *et al.*, Nucl. Instrum. Methods A 310, 577 (1991).